Surface mass balance and climate of the Last Glacial Maximum northern hemisphere ice sheets: simulations with CESM2.1

Sarah L. Bradley[1], Raymond Sellevold[2], Michele Petrini[3], Miren Vizcaino[2], Sotiria Georgiou[2], Jiang Zhu[4], Bette L. Otto-Bliesner[4], and Marcus Lofverstrom[5]

[1]Department of Geography, The University of Sheffield, Sheffield, UK
[2]Geosciences and remote sensing, Delft University of Technology, Delft, the Netherlands
[3]NORCE Norwegian Research Centre AS, Bjerknes Centre for Climate Research, Bergen, Norway
[4]Climate and Global Dynamics Laboratory, National Center for Atmospheric Research, Boulder, CO, USA
[5]Department of Geosciences, University of Arizona, Tuscon, AZ, USA

Correspondence: Sarah Bradley (s.l.bradley@sheffield.ac.uk), Miren Vizcaino (M.Vizcaino@tudelft.nl)

Abstract. The Last Glacial Maximum (LGM, from ∼26 to 20 ka BP) was the most recent period with large ice sheets in Eurasia and North America. At that time, global temperatures were 5-7°C colder than today, and sea level ∼125 m lower. LGM simulations are useful to understand Earth System dynamics including climate-ice sheet interactions, and to evaluate and improve the models representing those. Here, we present two simulations of the Northern Hemisphere ice sheet climate and

5 surface mass balance with the CESM2.1(CAM5) with prescribed ice sheets for two time periods that bracket the LGM period: 26 ka and 21 ka BP. CESM2.1 includes explicit simulation of snow/firn compaction, albedo, refreezing, and direct coupling of ice sheet surface energy fluxes with the atmosphere. The simulated mean snowfall accumulation is lowest for the Greenland and Barents-Kara Sea Ice Sheets (GrIS, BKIS) and highest for British and Irish (BIIS) and Icelandic (IcIS) ice sheets. Melt rates are negligible for the dry BKIS and GrIS, and relatively large for the BIIS, NAISC, SIS and IcIS, and are reduced by almost a

10 third in the colder 26 ka BP climate compared with 21 ka BP. The surface mass balance (SMB) is positive for the GrIS, BKIS, SIS and IcIS during the LGM (26 ka and 21 ka BP), and negative for the NAISC and BIIS. Relatively wide ablation areas are simulated along the southern (terrestrial), Pacific and Atlantic margins of the NAISC, across all of the BIIS surface, and along the terrestrial southern margin of the SIS. For 26 ka BP climate the integrated SMB substantially increases for the NAISC and BIIS, but it does not reverse the negative sign. Summer incoming solar radiation at the surface is largest over the high interior

15 of the NAISC and GrIS, and minimum over the BIIS and southern margin of NAISC. Summer net radiation is maximum over the ablation areas and minimum where the albedo is highest, namely in the interior of the GrIS, northern NAISC and all of the BKIS. Summer sensible and latent heat fluxes are highest over the ablation areas, positively contributing to melt energy. Refreezing is largest along the equilibrium line for all ice sheets, and prevents 40-50 % of meltwater entering the ocean. Our SMB results are in qualitative agreement with the climatic variability across the different northern hemisphere ice sheets. The

20 large simulated melt for the NAISC suggests potential biases in the climate simulation, ice sheet reconstruction, and/or highly non-equilibrated climate and ice sheet at the LGM time.

1 Introduction

Ice sheets play an important role in the Earth system through complex interactions with the atmospheric and oceanic circulation while simultaneously exerting a primary control on the global sea level (Fyke et al., 2018). The Greenland (GrIS) and
25   Antarctic (AIS) ice sheets are expected to become the largest contributor to future sea level rise. Projections of present-day ice sheet change and sea-level rise are primarily based on stand-alone ice sheet model simulations and/or regional climate modelling that provides robust representation of surface mass balance (SMB) change. However, neither of these modeling approaches include interactions between ice sheets and the global climate. Simulations of global climates with interactive ice sheets have been performed with intermediate complexity model (EMICS) or relatively low resolution AOGCMs including
30   simplified SMB schemes (Ziemen et al., 2014; Quiquet et al., 2021). The coupling of global climate and ice sheet models is challenging (Muntjewerf et al., 2021), mainly due to the relatively coarse resolution of climate models compared to the required high resolution for an ice sheet model, and the large computational expense of running long climate simulations over multi-millennial timescales (Lofverstrom et al., 2020). Significant development has been made in the last decade, for instance, with the first realistic simulations of SMB with global models (Vizcaíno et al., 2013), and more recently with the first realistic
35   simulations of SMB and ice discharge within an Earth System Model with interactive ice sheets (Muntjewerf et al., 2020b; Sommers et al., 2021; Lofverstrom et al., 2020, 2022).

    Here, we present Community Earth System Model version 2.1 (CESM2.1) simulations of the last glacial maximum (LGM) Northern Hemisphere ice sheets with a relatively high resolutionclimate component (∼1°) and an explicit calculation of ice sheet surface processes (melt energy fluxes, snow/firn compaction, albedo and refreezing evolution (Lawrence et al., 2019;
40   Sellevold et al., 2019). The LGM extended from 26 ka to 20/19 ka BP (Clark et al., 2009) and historically 21 ka BP has been used as the representative time period (Mix et al., 2001; Kageyama et al., 2017). During this 6 ka interval, atmospheric trace gases and ice core temperature records are relatively stable (see Fig.1, Ivanovic et al. (2016)), but the solar insolation signal is steadily increasing and the timing of the local LGM of the continental ice sheets was highly asynchronous. For example, the North American ice sheet complex (NAISC, (Laurentide, Cordilleran and Innuitian)) is inferred to have reached it maximum
45   extent at 25 ka BP. However, as the recent review by Dalton et al. (2022) highlights, regionally the LGM was asynchronous, earlier (ca. 27 ka BP) in the offshore region of western Canada, and later (ca. 18 ka BP) in the west. The Scandinavian (SIS) and Barents-Kara ice sheets (BKIS) coalesced and reached their maximum at 24 ka BP (Hughes et al., 2016) whereas the British and Irish and North sea ice sheet (BIIS) reached a maximum extent at 23 ka BP with rapid deglaciation initiated at 22 ka BP (Clark et al., 2022).

50   As previous studies have shown, modelling the LGM and maintaining a maximum glacial extent for both the NAISC and SIS has been problematic (Ziemen et al., 2014; Quiquet et al., 2021; Patton et al., 2016). Therefore, to investigate climate-ice sheet interactions during the LGM, an earlier time period within this 6 ka interval may be more representative. To this end, we present two simulations for the LGM, one for the onset of the LGM, 26 ka BP (LG-26ka) and one for the end, 21 ka BP (LG-21ka). Our aim is to provide a detailed simulation of the climate, surface energy fluxes and SMB components of the LGM

northern hemisphere ice sheets and evaluate the differences between the LG-21ka, the standard reference for the LGM period and the LG-26ka.

The paper is structured as follows. Section 2 describes the model and simulation design. Section 3 presents the simulation of global climate. Section 4 shows the analysis of the SMB of the ice sheets. Section 5 contains the discussion and conclusions.

2 Method

2.1 Community Earth System Model 2.1

All results in this paper are from CESM2.1 (CESM2.1; Danabasoglu et al., 2020), a model which includes components for the atmosphere, ocean, sea ice, land, and ice sheets. The model has participated in the Climate Model Intercomparison Project 6 (CMIP6). Of the CMIP6 models, it is the only model providing an interactive calculation of the Greenland ice sheet SMB for all simulations and dedicated interactive GrIS simulation (Sellevold and Vizcaíno, 2020).

The atmosphere is simulated by the Community Atmosphere Model (CAM; Danabasoglu et al., 2020) version 5 (CAM5) physics, combined with the sub-grid orographic form drag parameterization of CAM6. CAM5 physics was preferred over the standard CAM6 in CMIP6 simulations due to the CAM6 physics yielding unrealistically high cooling under last glacial forcings (Zhu et al., 2021). This excessive cooling (due to high equlibrium climate sensitivity) has been attributed to updates in cloud parameterizations introduced in CAM6 (Gettelman et al., 2019; Zhu et al., 2022). A detailed comparison of CAM5 and CAM6 simulation of contemporary polar climate is given in Lenaerts et al. (2019).

The land model used in our simulations is the Community Land Model version 5 (CLM5; Lawrence et al., 2019). We turn off the anthropogenic influence (e.g., harvesting and irrigation) on vegetation. We use the River Transport Model (RTM; Hurrell et al., 2013) rather than the default and more advanced Model for Scale Adaptive River Transport (MOSART), as the latter requires high-resolution input, which is not available for the LGM. CLM5 calculates the SMB over the ice sheets via an energy-balance calculated for melt and advanced simulation of snow and firn processes (van Kampenhout et al., 2017). The model simulates realistically simulates contemporary ice sheet climate and SMB (van Kampenhout et al., 2020) and has been applied to projections for the GrIS (Muntjewerf et al., 2020, Muntjewerf et al., 2020b, Sellevold et al., 2020). Sub-grid variations in the SMB are simulated with the use of ten elevation classes (Sellevold et al., 2019). These elevation classes are active in CLM5 grid cells where both the land ice model is active and there is land-ice present. We make two minor modifications to the default settings for the elevation classes parameterizations (van Kampenhout et al., 2020). The first modification is an increase of the bare ice albedo from 0.4 to 0.5. The former relative low albedo used in Greenland simulations (van Kampenhout et al., 2020) was partially motivated to account for the low albedo in the "dark zone" of the present-day southwestern ablation area. Second, we use different thresholds for repartitioning the precipitation phase between snow and rain. Precipitation falls exclusively as rain above $2°C$ and snow below $0°C$, with mixed-phase precipitation between this range. These repartition thresholds are the same as used over vegetation by default in CESM2.1.

The atmosphere and land model are ran at a horizontal resolution of 0.9° (latitude) × 1.25° (longitude); the ocean model (POP2) and sea ice model (CICE5) are ran on a 1° displaced Greenland grid. In the ocean model we do not include ocean biogeochemistry (MARBL) but the estuary model from Sun et al. (2017) is adopted.

The Community Land Ice Model version 2.1 (CISM2.1; Lipscomb et al., 2019) is used as a diagnostic component; i.e., we
90 do not run with interactive ice sheets. The 4-km CISM2.1 grid (Fig. A1) provides high-resolution information for CLM5's elevation classes, as well as downscaled SMB (at 4 km resolution) by horizontal bilinear and vertical interpolation from the elevation classes. In our simulations we produce elevation class information for SMB, surface air temperature across the CISM2.1 grid (Fig. A1) of the Northern Hemisphere ice sheets but also across the Antarctic and Patagonia ice sheets (however the latter are not analysed here).

2.2   Model set up and boundary conditions

We ran two 500 years-long simulations for 26 ka BP (LG-26ka) and 21 ka BP (LG-21ka) using the boundary conditions and glacial forcings listed in Table 1. The LG-21ka simulation was initialised using two published 21 ka CESM simulations for the climate and ocean. The climate and ocean state at year 100 of LG-21ka was used as the initial conditions for LG-26ka. An offline glacial isostatic adjustment model (GIA, see general description in Whitehouse (2018)) was ran to produce the
100 initial 21 ka input boundary conditions which define the paleocoastlines, topography, land-ocean mask and ice sheet extent. The input ice sheet reconstruction used for the GIA model combines the Antarctic and Patagonia ice sheets from ICE5G (Peltier, 2004); the North American ice sheet complex (NAISC, Laurentide (LIS), Cordilleran (CIS) and Innuitian (IIS)) from GLAC1D (Tarasov et al., 2012), the GrIS from HUY3 (Lecavalier et al., 2014), and the Eurasian ice sheet complex (British and Irish, Scandinavian and Barents-Kara Sea) from BRITICE-CHRONO (Clark et al., 2022) (Fig.A1). The GIA model output
105 was regridded to a reference 10 min grid (bilinear interpolation following the protocol as defined in PMIP4 (Kageyama et al., 2017, figure 3). An offline vegetation model (BIOME4; Kaplan et al., 2003) was ran with climate forcing from the LG-21ka simulation to generate the vegetation distribution (see Appendix B). The overflow parameterization in POP (Danabasoglu et al., 2010) was adjusted from the model modern values due to the narrowing of Denmark Strait as a result of the larger-than-present GrIS. Also, part of Baffin Bay was closed due to excessive sea-ice formation in connection with a narrower bay from the
110 larger-than-present GrIS. This part is treated as covered with land ice.

3   Climate simulation

To evaluate the climate state from our two simulations, we compare the global average of a range of climate outputs from LG-21ka and LG-26ka to published proxy and model results (Table 2). Additionally, we compare the spatial pattern of the global surface temperature (SAT) from LG-21ka with two different datasets: (i) an alternative 21ka CESM2.1 (Zhu et al., 2021, refer
115 to as LGM-Zhu) and (ii) proxy-constrained, full-field reanalysis from Osman et al. (2021) (refer to as Osman) (Fig. 1c+d). There are a number of differences in the model setup between the two CESM2.1 21 ka simulations (LG-21ka and LGM-Zhu): (i) the input vegetation dataset, with LGM-Zhu adopting a PI datasets all over the globe; (ii) the ice sheet reconstruction, with

Table 1. Summary of boundary conditions and forcings used for the two simulations. For the LG-21ka and LG-26ka values were taken from Ivanovic et al. (2016).

Parameter setting	LG-21ka	LG-26ka
Solar constant	pre-industrial	pre-industrial
Eccentricity	0.018995°	0.017742[1]
Obliquity	22.949°	22.31°[1]
Perihelion-180	114.42°	32.09°[1]
CO_2 (ppm)	190	184[2]
CH_4	375	355[3]
N_2O (ppb)	200	199[4]
Others (CFC)	0	0
Ozone	pre-industrial	pre-industrial
Vegetation	21ka[5]	21ka[5]
Land surface topography	21ka	21ka
Ice sheets	21ka	21ka
Ocean restart	CESM1 21ka[6]	LG-21ka
Climate restart	CESM2 21ka[7]	LG-21ka
Simulation length	500 years	500 years

[1] Berger (1978). [2] Bereiter et al. (2015). [3] Loulergue et al. (2008). [4] Schilt et al. (2010). [5] Offline BIOME4 simulation Kaplan et al. (2003). [6] DiNezio et al. (2018). [7] Zhu et al. (2021)

LGM-Zhu using the ICE6G as defined within the PMIP4 protocols. In this reconstruction, the GrIS is smaller and does not extend beyond the present day coastline. As such the adjustments made within POP in our model setup, narrowing of Baffin
120 Bay and adjustment of the overflow parameterization are not required.

An average global near-surface cooling of 6.84°C is simulated by the last two decades of the LG-21ka simulation (Fig. C1, Table 2), which agrees well with the results from the two comparison datasets; Osman 7±1°C and 6.5°C LGM-Zhu, and is significantly colder everywhere than in PI (Fig. 1a). The LGM shows polar amplification of cooling in both seasons, but strongest in the winter (Fig. C2). Most of the cooling, in both seasons, occurs over the ice sheets that are not present in the
125 PI simulation, due to the higher elevations and the change from vegetated surfaces to ice surfaces. This is in contrast with contemporary polar amplification of global warming, where the highest increases in winter near-surface temperatures take place over the Arctic Ocean. In the Northern Hemisphere summer, the 0 °C isotherm correspond well to the southern margin of the ice sheets (Fig. C2c).

When comparing the LG-21ka results to LGM-Zhu and Osman, we find some notable spatial differences (Fig. 1c,d). The
130 lower surface elevation across the ice sheet regions and narrowing of Baffin Bay (Fig. 1) results in a cooling in LG-21ka compared to LGM-Zhu (Fig.1c), up to 7°C across BKIS and 16°C in Baffin Bay. The differences across the surface of the

large ocean basins are small, less than $\pm 0.5°$C, but as Section 3.3 describes, there are differences in the deep ocean circulation. Relative to the Osman study, LG-21ka is colder across AIS and the southern ocean (up to 7 °C), but is warmer across central Pacific Ocean, North Atlantic (up 11°C) and the Arctic Ocean (8°C). The largest warm anomalies are across the Northern

135 ice sheet region, up to 20°C across the centre of the CIS and 12°C across LIS, the former of which coincides with highest standard deviations from the model ensemble, up to 9°C. There is an anomalous cold zone extending from the southern coast of Greenland relative to both comparison datasets, the extent of which coincides with relatively large summer Arctic sea ice extent (Section 3.2).

The LG-26ka simulation is 1.5°C colder than LG-21ka (global average), enhanced at higher latitudes, with a 4°C and 2°C

140 cooling at GRIP and VOSTOK ice core sites, respectively. The largest anomalies are concentrated across the North Atlantic (decrease of 6°C) along the eastern margin of the GrIS and Siberia (decrease of up to 8°C) (Fig. 1b). In terms of the ice sheets, there is a cooling along the southern margin of the NAISC of 1°C, compared to 3°C across the BIIS, EuIS, and BKIS, which, as we evaluate in Section 4.1 has important implications for the simulated SMB.

Table 2. Annual-means of various quantities for the last 20-years of the simulations. LG-26ka and LG-21ka refers to our CESM2.1 simulation, CCSM4 to a simulation by Brady et al. (2013), PMIP4 to simulations by Kageyama et al. (2021), and Proxy to the different proxy data. Standard deviations are given in the curly brackets; differences to their respective PI simulations in brackets .

	LG-26ka	LG-21ka	CCSM4	PMIP4	Proxy
Global precipitation (mm day^{-1})	2.50 {0.01} (-0.58)	2.59 {0.01} (-0.49)	2.61 (-0.32)	2.72[1]	
Tropical precipitation (mm day^{-1})	3.26 {0.01} (-0.48)	3.32 {0.02} (-0.42)	3.93 (-0.36)		
Global near-surface T (°C)	6.47 {0.09} -8.30)	7.93 {0.11} (-6.84)	9.83[1]		6.40 (-7.10)[5]
Global surface T (°C)	7.39 {0.09} (-8.26)	8.86 {0.11} (-6.79)	9.04 (-4.97)	11.54[2]	
Tropical land surface T (°C)	21.42 {0.16} (-4.42)	22.28 {0.18} (-3.56)	20.89 (-2.61)		(-3.9)[8]
GRIP (°C)	-42.38 {1.51} (-14.39)	-38.35 {1.48} (-11.36)	-37.76 (-8.54)		(-11.5)[7]
Vostok (°C)	-62.35 {0.58} (-12.39)	-60.31 {0.72} (-10.35)	-62.84 (-9.97)		(-12)[6]
Global precipitable water (mm)	17.14 {0.10} (-8.69)	18.30 {0.18} (-7.53)	18.84 (-5.09)		
Tropical SST (°C)		23.14 {0.14} (-3.35)	24.78 (-2.16)	23.30[3]	(-3.5)[8]
AMOC at 30°N (Sv)	17.1	18.4	22	16-24	
Sea-ice area NH (×10^6 km^2)	12.54 {0.39} (2.74)	9.39 {0.21} (-0.41)	8.64 (-3.06)		9.40[4]
Sea-ice area SH (×10^6 km^2)	29.65 {0.47} (20.65)	25.87 {0.41}(16.87)	27.88 (10.9)		24.72[4]

[1] AWI-ESM-1-1-LR, INM-CM4-8, MIROC-ES2L, MPI-ESM1-2-LR. [2] MIROC-ES2L
[3] MIROC-ES2L, MPI-ESM1-2-LR .[4] Paul et al. (2021).[5] Osman et al. (2021).[6] Petit et al. (1999). [7] Lecavalier et al. (2014).[8] Tierney et al. (2020)

3.1 Atmospheric simulation: radiation, clouds and circulation

145 The top of the atmosphere insolation (TOA SW$_{in}$) that forces the 21 ky climate is substantially different from pre-industrial, due to the different orbital conditions. The LG-21ka simulation TOA SW$_{in}$ is reduced (less insolation) with respect to PI at
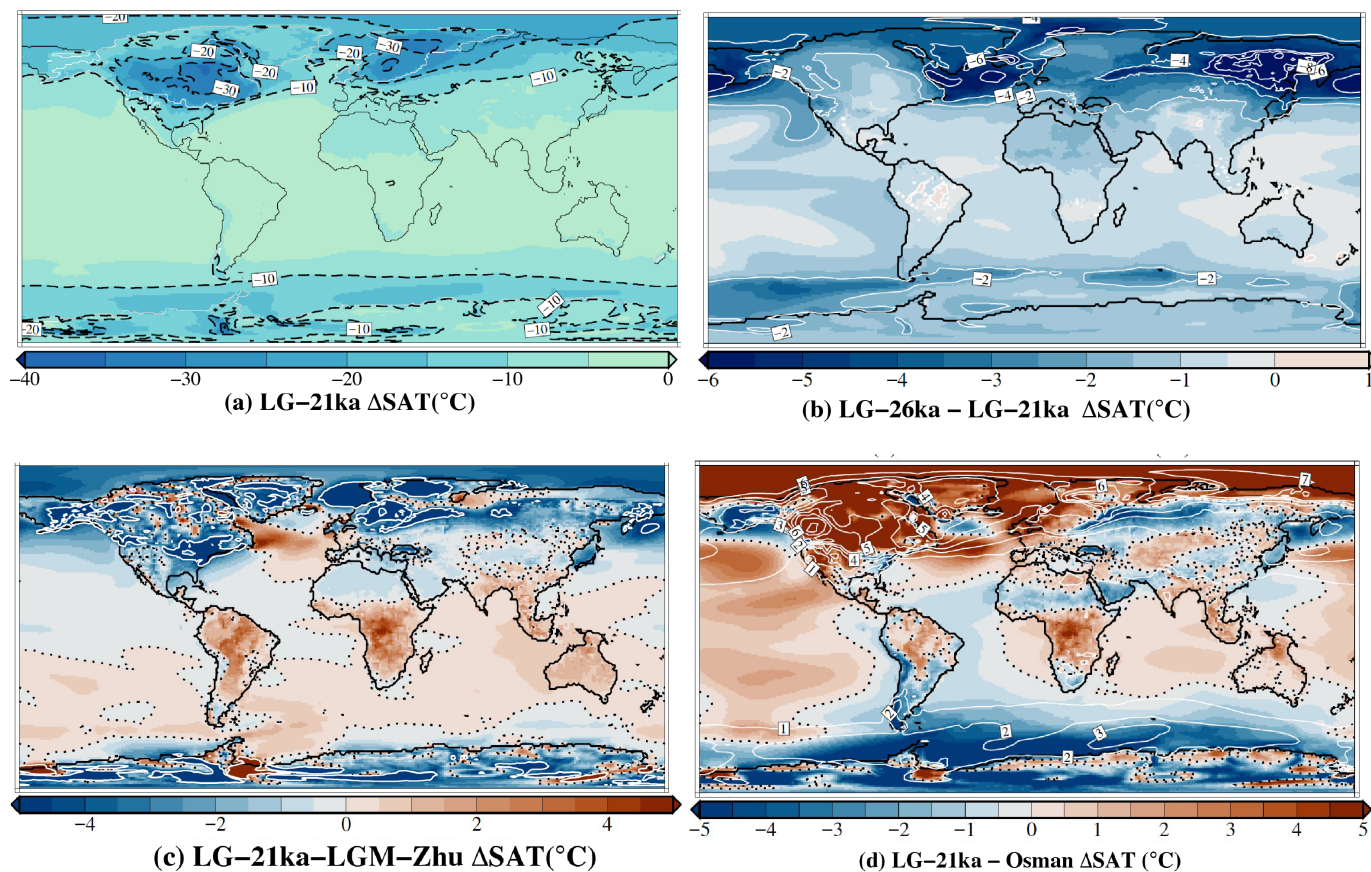
Figure 1. Annual-mean (20 years) near-surface air temperature (SAT °C) anomalies with respect to pre-industrial for (a) the LG-21ka simulation (30 yr average).The black contour is the paleocoastline, the white contour encloses the glaciated regions and the dashed-black contour lines are every 10°C. (b) Differences between LG-26ka and LG-21ka. Solid white contours are every 2°C. (c) Difference LG-21ka and LGM-Zhu, dotted black contour is the 0°C;White contour marks 5°C.(d) Difference between LG-21ka and SAT taken from Osman et al. (2021) (regridded to the CESM grid). Dotted black contour is the 0°C; The white contours are the standard deviation from the model ensemble, 1°C interval.

northern and southern high latitudes during May-October and October to March, respectively. Tropical and subtropical regions experience a small positive change in insolation for most months, except between August-October where they have a small negative change in insolation. During the periods of reduced TOA SW_{in} at northern and southern latitudes, there is an increase

150 in the surface SW_{in} (Fig. 2a). Changes in atmospheric and surface conditions explain these and other large differences between TOA and surface SW_{in}. By comparing differences in the SW_{in} flux under all-sky and clear-sky conditions (Fig. 2a,b), we find that the changes in cloud cover are the main contributor to the larger surface SW_{in}. In addition, the presence of the extensive LGM ice sheets (Fig. A1), as well as sea-ice extending further into the midlatitudes (see section 3.2) increase the surface albedo (see Fig. 9f). This increase allows for more multiple scattering and thereby increases surface SW_{in}. Furthermore, the

155 colder LGM atmosphere holds less water vapor (Table 2), also contributing to increases in the surface SW_{in}. In all high latitude regions showing enhanced surface SW_{in}, SW_{net} is however reduced due to overcompensation from higher surface albedo (Fig. 2c).

The surface incoming longwave radiation (LW_{in}, Fig. 2d) is reduced at all latitudes and times of the year with respect to PI with the largest anomalies corresponding to the areas of largest cooling over the ice sheets and expanded sea-ice cover. The

160 temporal and latitudinal pattern of surface net longwave radiation (LW_{net}, Fig. 2e) shows both positive and negative anomalies (positive corresponds to net radiation gain by the surface), with net radiation loss over the northern hemisphere ice sheets during the summer, and in the Tropics all over the year. The magnitude of this summer reduction in LW_{net} over the ice sheets is smaller than for SW_{net}.
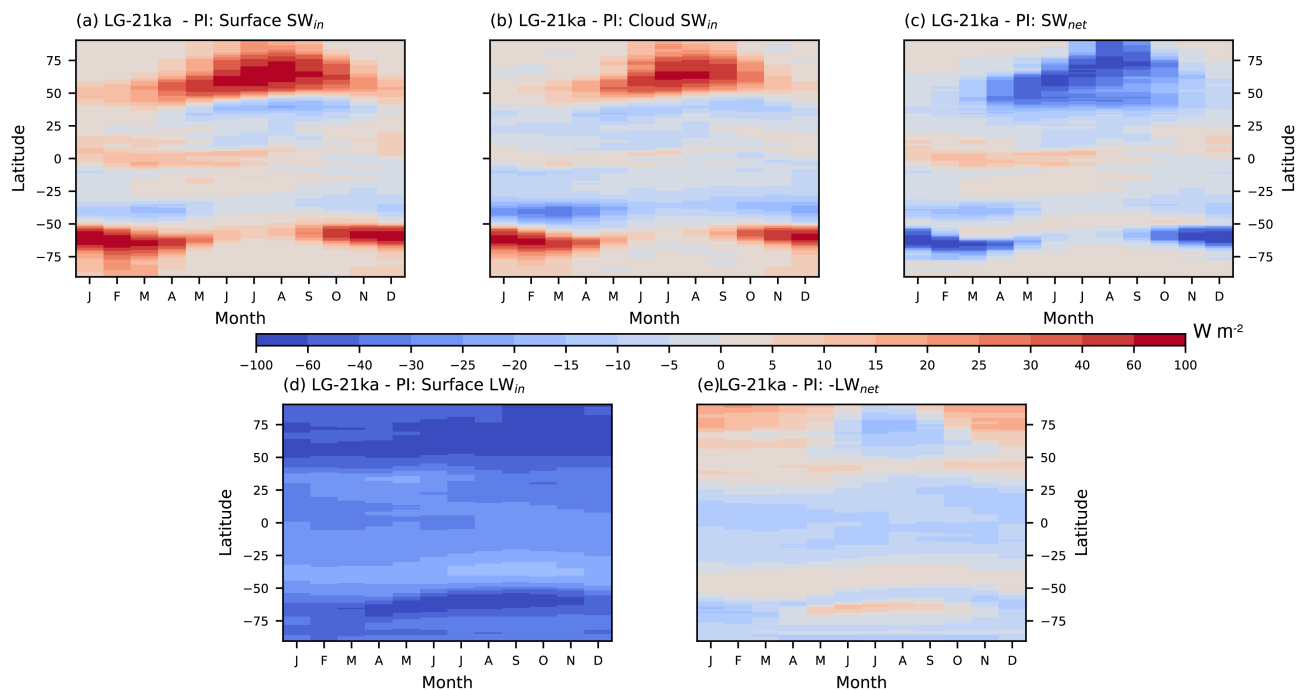
Figure 2. Monthly zonal means (20 years) of (a) incoming solar radiation at the surface (SW$_{in}$), (b) cloud contribution to incoming solar radiation at the surface (SW$_{in}$), (c) net shortwave radiation at the surface (SW$_{net}$), (d) incoming longwave radiation at the surface (LW$_{in}$), (e) net longwave radiation at the surface (LW$_{net}$). For all panels, positive values (red) indicate energy gain by the surface. Total radiation change at the surface results from the addition of panels c and e.

We continue our analysis of atmospheric change by examining changes in the atmospheric circulation and their connections with cloud change. To this end, we compare changes in the asymmetrical component of the geopotential heights between LG-21ka and PI (Fig. 3). Around the NAISC, two circulation anomalies appear (Fig. 3a+b). On the western side across the CIS, the PI winter ridge is intensified and extends further towards Asia. The winds associated with this ridge transports warm and moist air from the Pacific to Alaska. On the eastern side, across LIS, a negative response occurs, due to the strengthening and southward elongation of the Greenland climatological low, extending the persistent inflow of Arctic air towards the North Atlantic margin. This response strengthens the geopotential gradient between the Atlantic and LIS, suggesting higher wind speeds of the polar jet.

The winter climatological ridge (Fig. 3a) which brings warmer and moister air from the North Atlantic towards Europe is weakened along its northern flank, which results in drier and colder Arctic air over Northern Europe. On the Asian side, the Aleutian low is weakened. The summer circulation responses (Fig. 3b) are weaker than in winter. There is a negative response over LIS, which represents a narrowing of the Rocky mountain ridge and a strengthening and enlarged Greenland low. This change in summer circulation produces the colder condition over LIS during the LGM (Fig. 1a). There is a positive response

in the North Atlantic which extends across the BIIS. As both these responses strengthen the PI climatological features, they sharpen the geopotential gradients and give rise to higher wind speeds, which is indicative of increased synoptic eddy activity.

We find similar circulation anomalies in the LG-26ka simulations and as such, suggest that these features may be caused by
180   a combination of several factors, such as differences in land-sea configuration, topography, as well as thermal contrasts.

As we saw, clouds play an important role in regulating surface radiation fluxes. Cloud effects largely depend on their liquid water (efficient at blocking incoming solar radiation) and ice (nearly transparent to incoming solar radiation) content. During the summer, there is very little cloud liquid water across the ice sheets (Fig. 3c), a significant reduction compared to the PI (Fig. 3d). This is caused by the increase in elevation, a relatively high cloud liquid water in the PI, as well as negative circulation
185   anomalies making these areas receive more dry and cold Arctic air. Conversely there is an increase in cloud ice water (Fig. 3e+f), a feature that is common over current ice sheets, due to the colder temperatures and higher elevation (Ettema et al., 2010; Lenaerts et al., 2019).

The amount of annual mean precipitable water (i.e., the vertically integrated atmospheric humidity) decreases everywhere with respect to PI, and globally at 21 ka BP by 7.53mm (0.18 s.d) (Table2 and Fig. 4b). This is a consequence of the global
190   cooling, as a colder atmosphere can hold less water. The largest decreases occur in the tropics and over the southern parts of the ice sheets. The large reduction in the tropics is due to the relatively high amounts of precipitable water there in the PI. Over the ice sheets, the large reduction in precipitable water relates to large elevation change and cooling.

Although precipitable water decreases everywhere, some areas experience higher annual mean large-scale precipitation rates. We focus on large-scale precipitation (Fig. 4c), as this is the main process for generating precipitation over the ice sheets,
195   with convective precipitation playing a much smaller role. Increases in precipitation occurs along the southern margins of the NAISC, BIIS and SIS (Fig. 4d). These increases are likely associated with changes in circulation. As seen earlier, there is more advection of Pacific air, which increases precipitation. On the eastern margin of the LIS, we see increase of wind speeds, which can indicate more synoptic activity. Further, the steep and higher elevation together with the associated cooling inwards on the ice sheet, can force precipitation to fall at the margins. Over the SIS, synoptic systems move, on average, more along the margin
200   of the ice sheet, while in PI they could move further north. This possibly explains the response of increased precipitation along the margins and the drier conditions in the North.

In summary, we see large differences in circulation, clouds, temperature, and precipitation between the LG-21ka and PI climates, some of them largely connected with the presence of large ice sheets in the northern hemisphere. The circulation in LG-21ka suggests more advection of Pacific air towards Alaska, bringing more moisture which increases precipitation
205   and thickens clouds. The interior of the Laurentide experiences an anomalous trough, which likely brings in drier Arctic air, leading to thinning of clouds, less precipitation, and much colder air temperatures than in PI. In LG-21ka colder conditions are simulated around Greenland, particularly in the West where the PI low gets strengthened. The Eurasian ice sheets experience similar responses as the Laurentide: wetter in the south, drier in the interior and north.
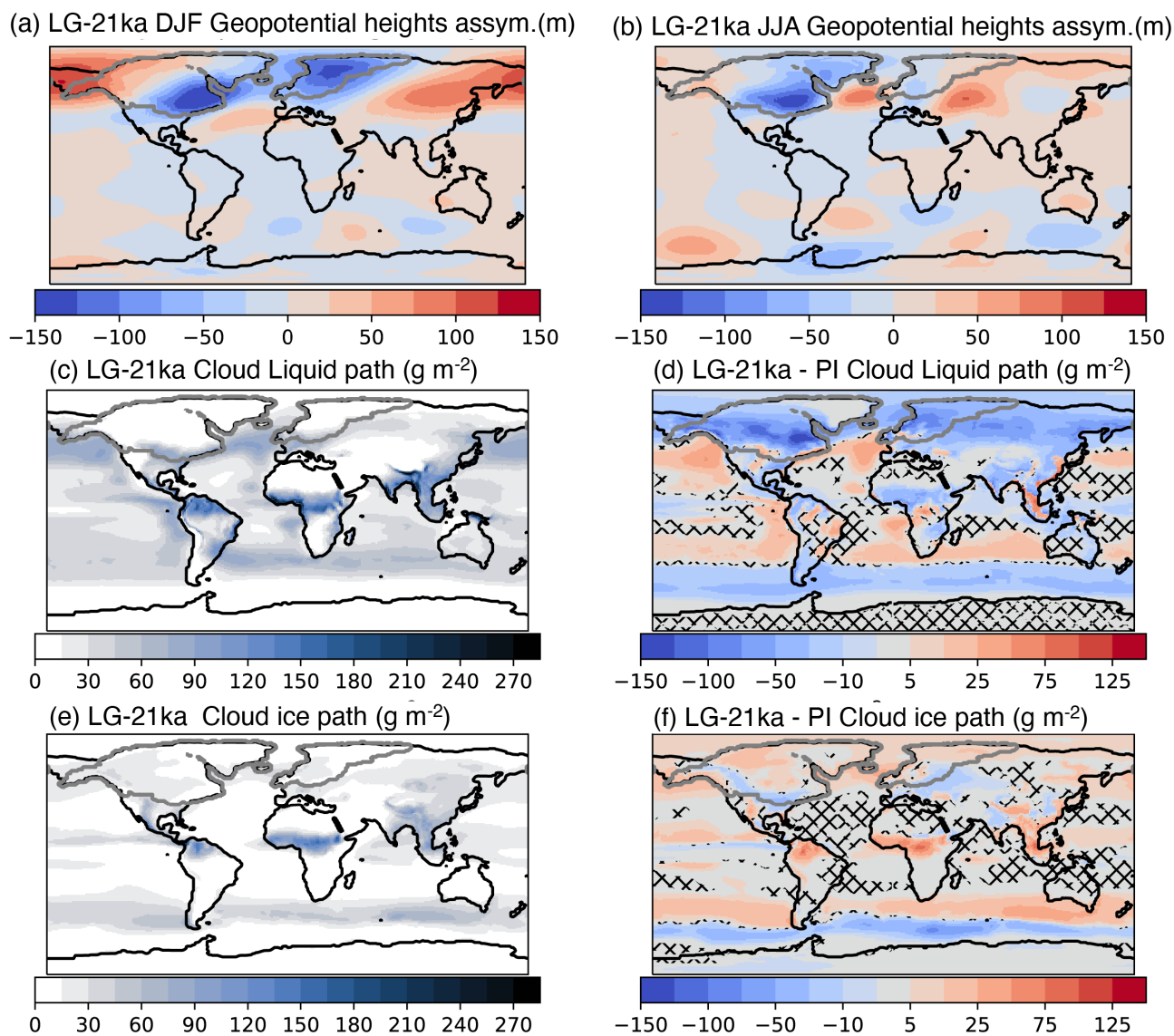
Figure 3. Geopotential height anomalies (relative to PI) (m) after subtracting the zonal means (20 years) (a) DJF and (b) JJA. Panels (c - f) are relative to the Summer mean clouds. (c) and (d) shows cloud liquid path, while (e) and (f) shows cloud ice path, all in g m^{-2}. The left column shows values from the LG-21ka simulation, while the right column shows the differences between LG-21ka and the PI simulations. Grey contour encloses glaciated areas (>50% ice cover). Patched areas show where differences are non-significant at the 99% level according to a student's t-test relative to the month variations.
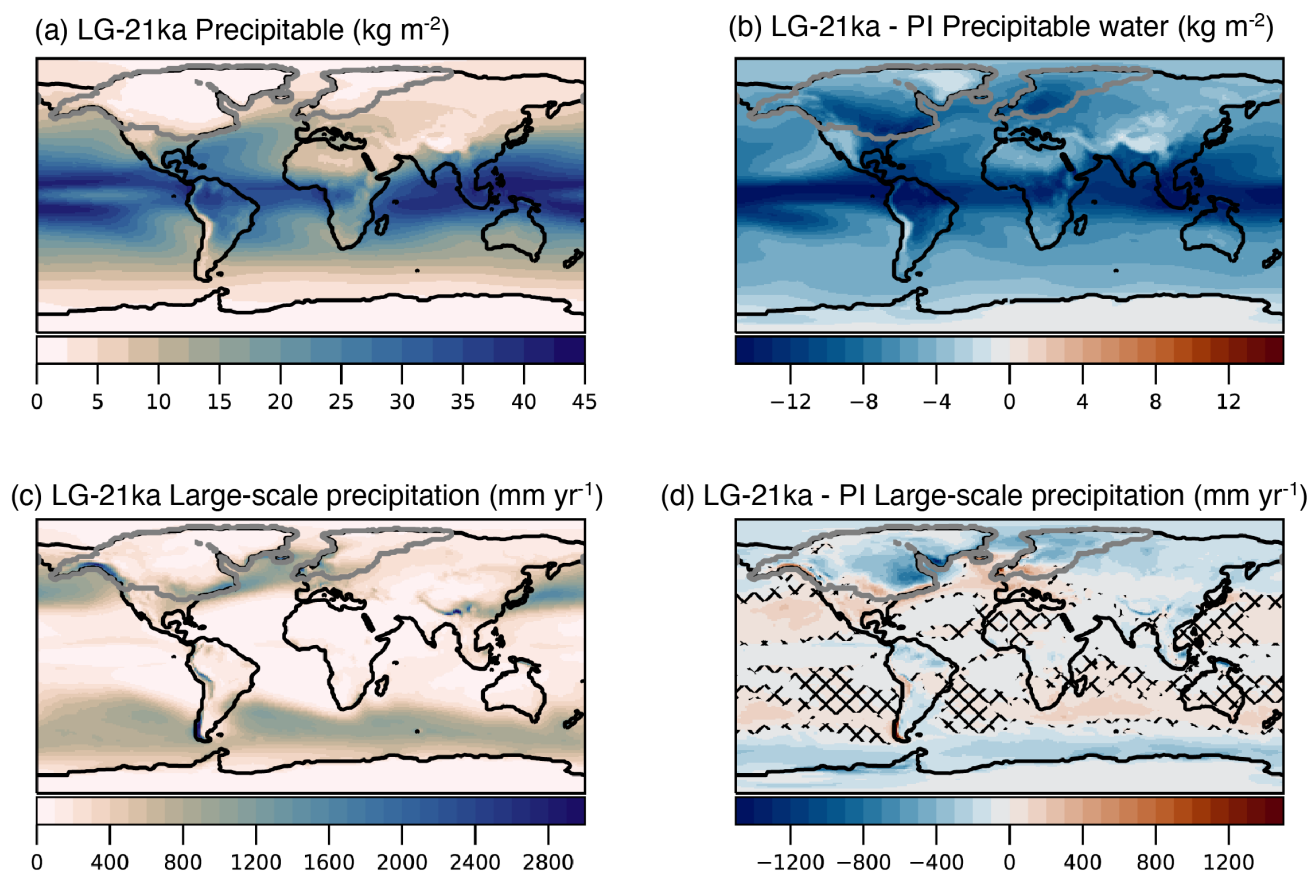
Figure 4. Annual means (20 years) for atmospheric water content. a) and b) shows precipitable water (kg m^{-2}), while c) and d) shows large-scale precipitation (mm yr^{-1}). The left column shows values from the LG-21ka simulation, while the right column shows the differences between LG-21ka and the PI simulations. Grey contour encloses glaciated areas (>50% ice cover). Patched areas show where differences are non-significant at the 99% level according to a student's t-test.
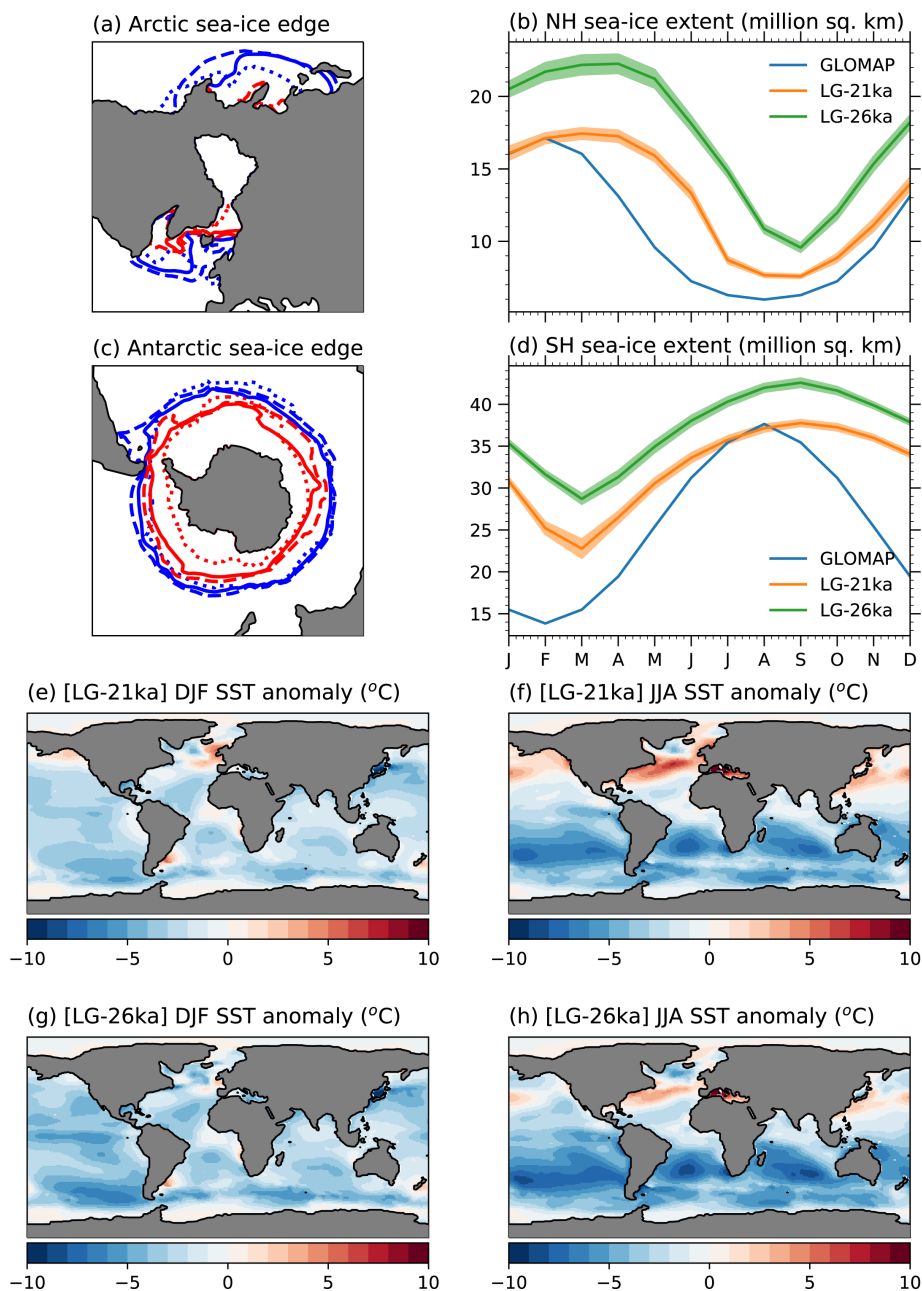
Figure 5. Comparison of sea-ice and SSTs between LG-21ka and LG-26ka and GLOMAP (Paul et al., 2021). (a,c) Shows sea-ice edge (>15% sea-ice concentration) for the maximum/winter extent (blue) and minimum/summer extent (red), with LG-21ka in solid lines, LG-26ka dashed line and GLOMAP dotted lines. (b,d) Shows the mean (20 years) sea-ice extent for the Northern and Southern Hemispheres per month of the year. (e-h) Shows the DJF and JJA SST anomalies (°C), where the anomalies are the difference between LG-21ka and LG-26ka and GLOMAP, and their respective pre-industrial values.

3.2 Sea surface conditions

210 To evaluate the ocean from our simulations, we compare our LG-21ka against sea surface temperatures (SSTs) and sea-ice extent from a global climatology of the ocean surface during the LGM mapped on a regular grid (Paul et al., 2021) (refer to as GLOMAP, where the LGM is defined as the interval between 23ka and 19ka BP). Both the Northern and Southern Hemisphere global average sea-ice area from LG-21ka are overestimated relative to GLOMAP, with the area increasing in the colder LG-26ka simulation (Fig. 5b+d, Table. 2). When comparing the Northern Hemisphere monthly variability (Fig. 215 5b), the timings of our maximum (March) and minimum (September) extent matches the case for the present-day but are one month later than recorded by GLOMAP, February and August respectively. There is a similar difference in the timings of the maximum/minimum in the Southern hemisphere monthly extents (Fig.5d).

For the Arctic region, there are some obvious differences between LG-21ka and GLOMAP. The summer sea-ice extent (compare red solid and dashed lines (Fig.5a)) is overestimated in our simulations, covering large parts of the Norwegian 220 and Greenland Seas, which are ice free in GLOMAP. In winter (compare blue solid and dashed lines (Fig. 5a)), LG-21ka overestimates sea-ice in the region south of Greenland, extending from Baffin Bay into the Labrador Sea, but underestimates across the Norwegian and Greenland seas. Across the Pacific ocean, the summer sea-ice extent is small and agrees well with the GLOMAP ice free conditions. In winter, however, we overestimate within the Northwest Pacific, across the Bering Sea, but underestimate within the Gulf of Alaska, simulating sea-ice free conditions.

225 In the Southern Hemisphere, differences with GLOMAP are smaller, with the sea-ice extent within the Indian Ocean a closer match to the results from GLOMAP. Regardless of the season, our model overestimates the sea-ice in the Pacific sector, but underestimates in the Atlantic ocean in relationship with GLOMAP.

Generally, LG-21ka simulates colder ocean conditions than GLOMAP (Fig. 5e-f) across large areas of the ocean, with the global mean SST -2.2 °C and -2.4 °C colder in winter and summer respectively. This colder ocean may be one cause for 230 the consistent overestimation in the sea-ice extent. There are warm anomalies (reaching up to 8°C), which are predominately concentrated in the Northern hemisphere, extending from the NAISC across the North Atlantic to the BIIS and extending from the North Pacific ocean (the Gulf of Alaska and Bering Strait) across to the sea of Japan.

3.3 Atlantic Meridional Overturning Circulation

In a recent study within the framework of the Paleoclimate Modelling Intercomparison Project (PMIP4, Kageyama et al., 235 2021) it was found that most of the models of the PMIP4 ensemble simulate a weaker and shallower overturning cell than in the PMIP3 simulations but all are stronger than the PI. In this subsection, we evaluate the simulated glacial AMOC state and we discuss the AMOC response to changes in orbital forcing (i.e. LG-21ka and LG-26ka) and the prescribed glacial continental ice sheets (i.e. LGM-Zhu).

The simulated AMOC strength (defined as the maximum AMOC transport at 30°N) is in a rather stable state during the last 240 ∼200 years of all simulations (Figure 6a). In the following, we analyze averages of the last 20 years of each simulation.

The AMOC strength is weaker and the extent of the overturning cell shallower§ in all three LGM simulations relative to the PI (Figure 6b). The maximum strengths are 18.4 Sv, 17.1 Sv and 16.6 Sv for LG-21ka, LG-26ka and LGM-Zhu, (Figure 6b) respectively. As stated earlier, the LG-21ka and LGM-Zhu simulations adopted different ice sheet reconstructions from PMIP4: GLAC1d (modified, see section 2.2) and ICE6G respectively and the former has a revised circulation around Baffin
245 Bay and Denmark Strait due to the larger-than present GrIS. A recent publication (Kapsch et al., 2022) found that the ICE6G reconstruction resulted in a stronger AMOC, relative to GLAC1D due partly to higher elevation across the NAISC complex. This is opposite of the results from this comparison, which highlights the complex non-linear interplay between the change in elevation across NAISC and EuIS and the resultant impact on wind speed, sea-ice extent and AMOC strength (Sherriff-Tadano et al., 2018; Sherriff-Tadano and Abe-Ouchi, 2020; Zhu et al., 2014).

250 The maximum extent of the overturning cell, defined as the depth for which the AMOC strength (at ∼30°N) is positive, shoals by ∼240 m for LG-21ka and LG-26ka and by 480m in LGM-Zhu. (Figure 6b). The shoaling of the simulated glacial AMOC compared to the PI simulation is in agreement with most of the earlier LGM studies (e.g. Muglia and Schmittner, 2021; Gu et al., 2020).

The AMOC in a depth-latitude view highlights the above mentioned difference (all results are relative to PI) (Figure 6c-e).
255 These results also stress the importance when comparing publications to ensure the same definition for latitude and depth is adopted for the AMOC. South of ∼50°N the AMOC is weaker and shallower in all three LGM simulations (LG-21ka, LG-26ka and LGM-Zhu), while north of ∼60°N its signal is stronger and of similar vertical extent. Previous studies have suggested that the process of deep convection in the Labrador Sea is affected by the advancing of the sea-ice in the colder glacial climate and in turn impacts the AMOC strength and geometry (Klockmann et al., 2018). As stated above, this is a region where LG-21ka
260 overpredicts the extent of the sea-ice (Fig.5a). Indeed, the winter mixed layer depth averaged over the subpolar North Atlantic is shallower by ∼400 m in the glacial simulations compared to PI (Figure C3a-c). That means that in the glacial simulations the formation of deep water masses is limited in this region resulting in a weaker overturning cell compared to PI. However, in the Nordic Seas the winter mixed layer depth is deeper in the glacial simulations compared to PI (Figure (C3a-c) explaining the stronger AMOC signal that is evident north of ∼60°N (Figure 6c-e).

265 In summary, we found that by changing the orbital forcing (i.e. LG-21ka and LG-26ka) the AMOC strength weakens possibly due to a reduction of the winter mixed layer depth in the North Atlantic led by an increase of the sea-ice (Figure 6a-b, and Figure C3d, Figure C4d). However, the vertical extent of the overturning cell is similar between LG-21ka and LG-26ka. Two recent transient simulations for the LGM period found either no change in the AMOC between 26 ka and 21 ka BP (Kapsch et al., 2022) or a minor weakening (Quiquet et al., 2021).

270 ## 4 Northern hemisphere ice sheet surface mass and energy balance

In the following, we will compare the SMB and summer surface energy balance and their components across the main continental scale northern hemisphere ice sheets. We distinguish between six ice sheets: NAISC, GrIS, BKIS, SIS, BIIS and Icelandic (IcIS). The summer energy balance is analysed to identify the different contributions from incoming solar and long-
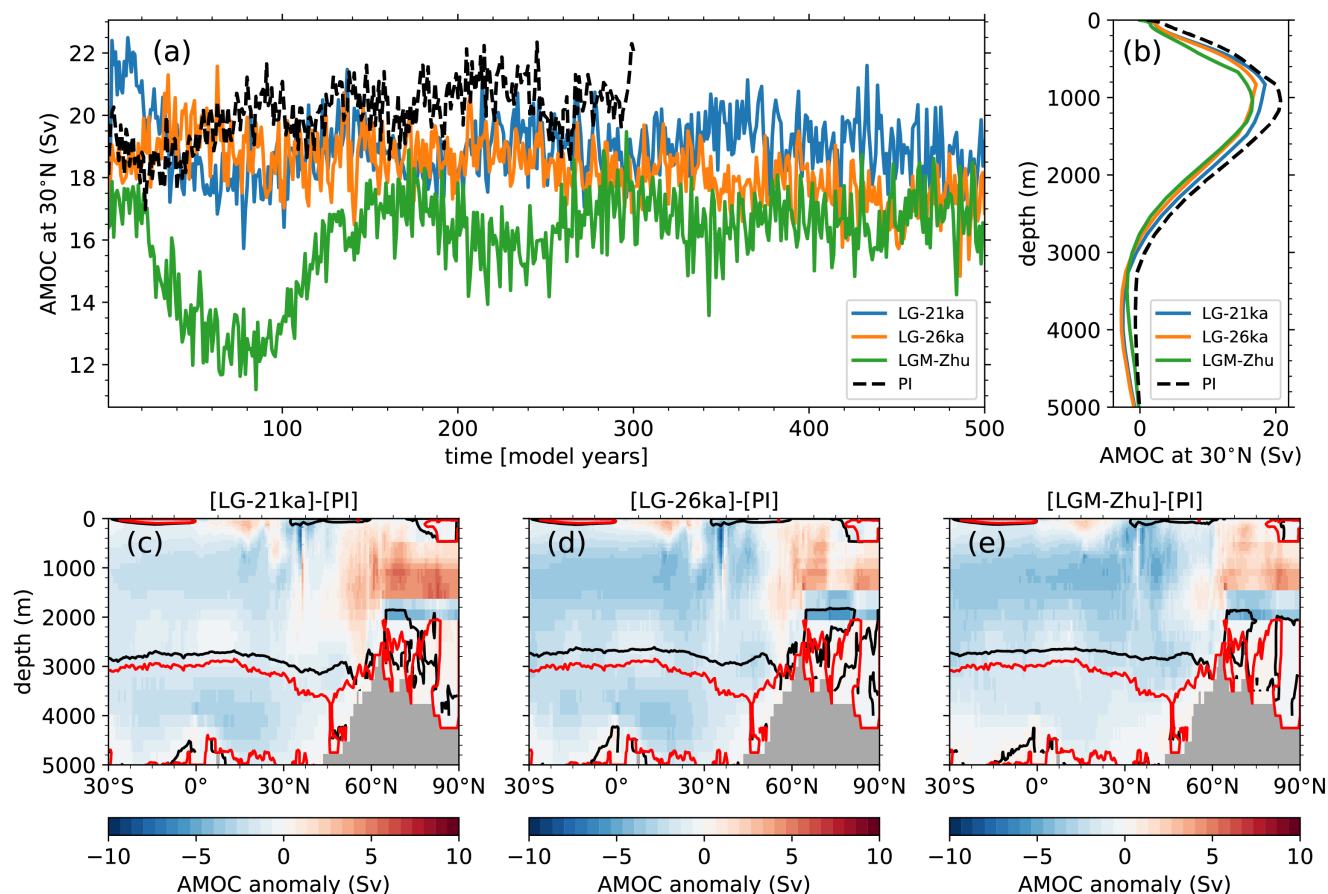
Figure 6. AMOC strength (defined as the maximum AMOC transport at 30°N) as a function of (a) time and (b) depth for LG-21ka (blue line), LG-26ka (orange line), LGM-Zhu (green line) and PI (black line). (c-e) AMOC anomaly as a function of latitude and depth (in Sv; 0 Sv contour line in black for LG-21ka and in red for PI) for (c) LG-21ka, (d) LG-26ka and (e) LGM-Zhu with respect to the PI simulation. Values in (b-e) are averaged over the last 20 years of each simulation.

wave radiation, albedo and turbulent heat fluxes to melt energy. In the last subsection, we compare the results of LG-26ka and LG-21ka.

4.1 Surface mass balance and components per ice sheet

Figure 7 shows a comparison of the spatially-averaged SMB and its components across the six major northern hemisphere ice sheets with the corresponding values for the present-day ice sheets of Greenland (Noël et al., 2020) and Antarctica (Mottram et al., 2021). Average values have been chosen to compare different ice sheets regardless of their different areas.

The averaged SMB of the IcIS, SIS, GrIS and BKIS is positive, with the latter two results of similar value to present-day Greenland and Antarctica (around 200 mm/yr). The similarity in the simulated mean GrIS SMB is the result of the almost
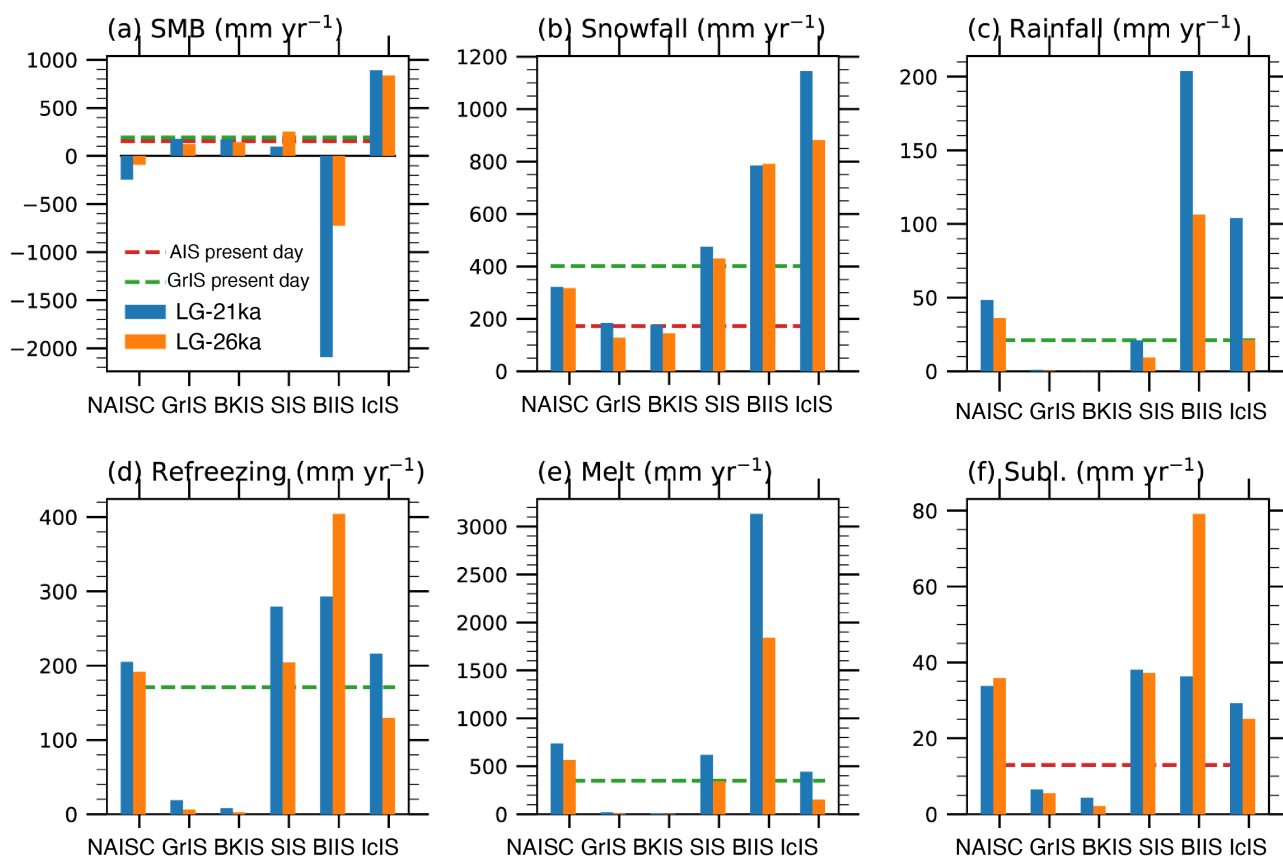
Figure 7. Annual means from the last 20 years of simulation of a) surface mass balance, b) snowfall, c) rainfall, d) refreezing, e) melt, and f) sublimation, all in mm yr^{-1}. Blue bars represent LG-21ka averages while orange bars represent LG-26ka averages, over the individual ice sheets. North American ice sheet complex (Laurentide,Cordilleran and Innuitian (NAISC)), Greenland ice sheet (GrIS), Barents-Kara Sea ice sheet (BKIS),Scandinavian ice sheet (SIS), British-Irish and northsea ice sheet (BIIS), and Icelandic ice sheet (IcIS). The green and red dashed line correspond to present day GrIS and AIS averages (Mottram et al., 2021; Noël et al., 2020). Note the annual means are scaled by ice sheet area (in units of mm yr-1).
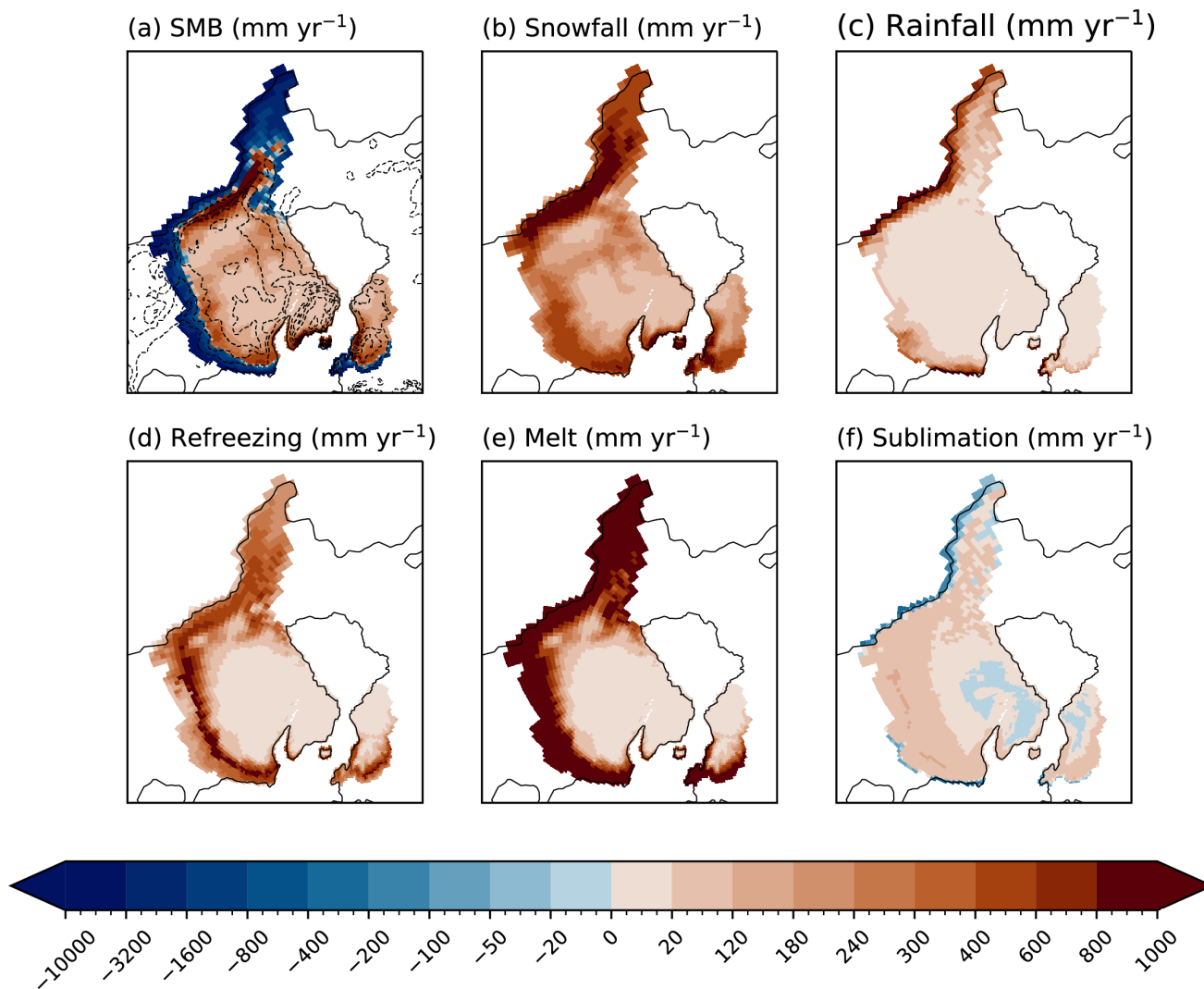
Figure 8. Maps of LG-21ka annual means from the last 20 years of simulation of (a) surface mass balance, (b) snowfall, (c) rainfall, (d) refreezing, (e) melt, and (f) sublimation, all in mm yr^{-1}.

zero melt rate (Fig. 7e) at the LGM combined with the 50% reduction in the snowfall rate (200mm/yr at the LGM versus 400 mm/yr for present-day, Fig. 7b). These differences in the SMB components are associated with the colder and drier LGM climate (Fig.4 and Fig.1).

285 The LG-21ka GrIS excluding the wetter southeast margin (Fig. 8b) and BKIS have similar mean SMB and components: low snowfall rates, zero rainfall and melt (except for a narrow band in southwest Greenland) and interiors with low net snow deposition (Fig. 8b) contrasting with low sublimation-dominated margins (Fig. 8f). All other ice sheets have large areas of melt which largely correspond with the relatively wide ablation areas (Fig. 8a and e). The SIS has a mean SMB that is half of the BKIS, regardless of more than double the snowfall rates (Fig. 7b), with a value very similar to present-day Greenland. This is 290 due to relatively large melt rates (almost double than for present-day Greenland). The SMB of the IcIS is the largest of all the six ice sheets, due to very high snowfall rate (Fig. 7b) that is only partially compensated by melt rates of a similar magnitude to present-day Greenland.

Two ice sheets have a extremely negative SMB: NAISC and BIIS. The CIS has a wide ablation area along the southern and western (Pacific) margins, with the latter corresponding to the high snowfall accumulation rates over the high elevation of the 295 Sierra Nevada mountain range (Fig. 8b). For the LIS, the high ablation and melt area extends along the entire southern margin, even over the relative high elevation of the southern (Atlantic) margin, due to the relatively warmer summer temperatures (Fig. C2). High refreezing rates are simulated along the equilibrium line altitude along the southern margin (Fig. 8d). Both these ice sheets (CIS and LIS) have high rainfall rates and inverse sublimation (or snowfall deposition) along the marine terminating margins not bordered by sea ice (see Fig. 5a), with mean values more than double present-day Greenland and Antarctica 300 respectively (Fig. 7c and f). The BIIS has the lowest mean SMB of the six ice sheets, despite of the second largest snowfall accumulation after the IcIS. The simulated ablation areas cover most of the ice sheet except for a minimal accumulation area in the interior, across the higher elevation of Scotland (Fig. 8a). The entire ice sheet surface melts seasonally (Fig. 8e), with average melting rates almost an order of magnitude larger than for the present-day Greenland.

If the simulated SMB, including the very wide and negative ablation area of the NAISC and BIIS, was applied to a dynamic 305 ice sheet model (for example,CISM2.1, Lipscomb et al. (2019)) it would be highly unlikely/challenging that the spatial extent of the southern margin in either ice sheet would be maintained; rapid retreat would occur. However, as outlined in section 1, the timing of the last glacial maximum for both these ice sheets was earlier than the historical 21 ka BP definition. (25 ka BP for NAISC, 23 ka BP for BIIS). Therefore, an earlier time step in this 6 ka period may be more appropriate to simulate the glacial maximum for these ice sheets. For this reason, in section 4.3, we compare the LG-21ka simulation with LG-26ka.

310 **4.2 Melt sources: the surface energy budget**

Here we will examine the components for the summer (JJA) energy budget over all northern hemisphere ice sheets (Fig.9). Melt is simulated across all margins of the major six continental ice sheets (Fig. 9a) apart from those bordered by sea ice (Fig. 5), for example the BKIS, the eastern margins of GrIS and the arctic sea margin of the LIS.

Incoming solar radiation is high in the interior of the NAISC, GrIS and SIS with much lower rates at the margins (Fig. 9b). 315 Minimum incoming solar radiation is simulated over the southern and Atlantic margins of the NAISC and over the BIIS, due

to higher amounts of cloud water over those ablation areas. An increase in shortwave radiation towards the higher elevation in the interior of ice sheets is also a feature of the present-day GrIS (van den Broeke et al., 2008) and is simulated by regional (Ettema et al., 2010) and global climate models (van Kampenhout et al., 2020; Vizcaíno et al., 2013; Dunmire et al., 2022) Conversely, maximum incoming longwave radiation is simulated over the lower, warmer margins of the ice sheets, except for
320   northern North America, GrIS and BKIS (Fig. 9c).

Summer surface albedo (Fig. 9f) is minimum (between 0.5 and 0.55) over the ablation areas corresponding to bare ice exposure. The highest albedo values (>0.80) correspond to dry snow areas extending from northern Canada, where the LIS and IIS coalesce, into central and SE Greenland, the IcIS high interior and most of the BKIS. The combination of this spatial albedo pattern and the reduction in incoming solar radiation over the ablation areas (Fig. 9b), results in maximum net solar
325   radiation over the southern regions of NAISC and SIS ice sheet margins (Fig. 9d). The sensible heat flux (SHF) provides energy for the surface over most of the ablation areas and all over Greenland. The largest flux towards the atmosphere is simulated at intermediate elevations, just above the equilibrium line altitude of the southern half of the NAISC. The latent heat flux (LHF) is positive (directed towards the surface) over a somewhat narrower band than the sensible heat flux along the lowest part of the ablation areas and is negative over the rest of the ice sheets. The ground heat flux (GHF) provides energy to the surface
330   along the areas with maximum refreezing (c.f Fig. 8d and Fig. 9i), due to the heat released in the refreezing process.

4.3   LG-26ka versus LG-21ka surface mass balance

The LG-26ka simulation results in a SMB increase with respect to LG-21ka for the NAISC, BIIS and SIS (Fig. 7 and Fig. 10a), with the largest absolute difference for the BIIS. However, for the NAISC and BIIS this does not reverse the SMB sign. This increase is primarily caused by a reduction in the melt rates (Fig. 7e and Fig. 10e). Over the BIIS, a small increase in snowfall
335   contributes secondarily to higher SMB, and is related to a cooling-related reduced fraction of precipitation falling as rainfall (Fig. 7c and 10b). Over the other five ice sheets, snowfall rates are lower in the LG-26ka simulation compared with LG-21ka. Mean rainfall rates decrease over all ice sheets, apart from the two driest (GrIS and BKIS) where it remains almost zero. The largest reduction is over the ice sheets with a prominent North Atlantic climate (BIIS and IcIS).

The SMB is lower in LG-26ka with respect to LG-21ka for the two ice sheets with almost zero melt (GrIS and BKIS) and
340   the IcIS, that has relatively low average melt rates. This decrease is due to reduced snowfall (Fig. 7b). A fall in melt rates at LG-26ka results in a refreezing reduction over all ice sheets except for the BIIS, where the combination of a large reduction in melt and rainfall and a minor increase in precipitation results in an increase in refreezing (Fig. 7d and Fig. 10d). Spatially (Fig. 10a), the SMB increases over the ablation areas and decreases in the accumulation areas, the latter due to reductions in snowfall (Fig. 10b). Snowfall increases and rainfall decreases along the western margin of the NAISC, in connection with colder temperatures (Fig. 1b). Refreezing increases over the ablation areas, in connection with a cooling-induced increase in the refreezing capacity, and decreases over the percolation areas, as a result of the reduction in melt (Fig. 10d and e).
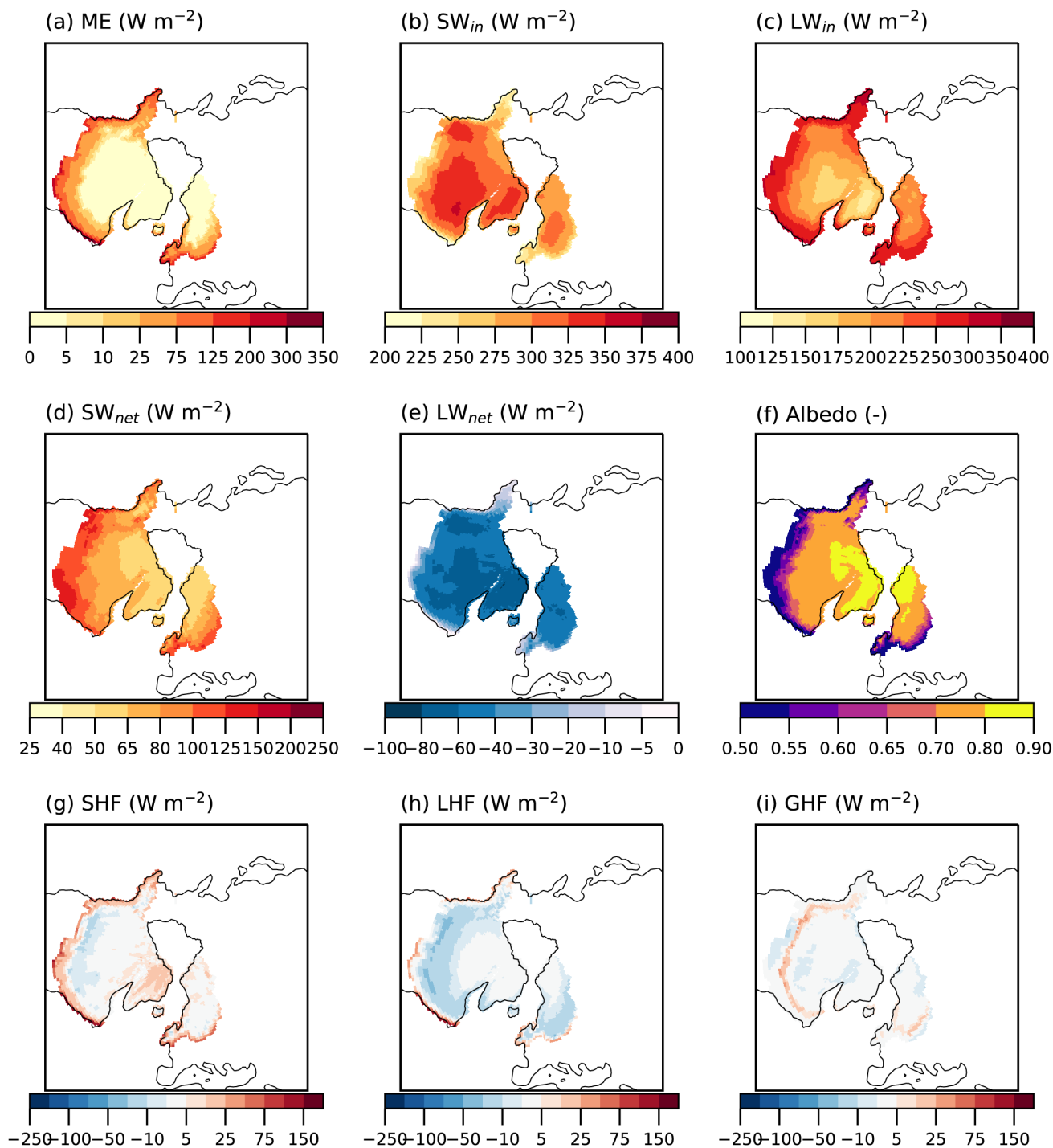
Figure 9. Maps of LG-21ka summer (JJA) means from the last 20 years of simulation of (a) melt energy (ME) (W m^{-2}), (b) SW$_{in}$ (W m^{-2}), (c) LW$_{in}$ (W m^{-2}), (d) SW$_{net}$ (W m^{-2}), (e) LW$_{net}$ (W m^{-2}), (f) albedo (-), (g) sensible heat flux (SHF) (W m^{-2}), (h) latent heat flux (LHF) (W m^{-2}), and (i) ground heat flux (GHF) (W m^{-2}).
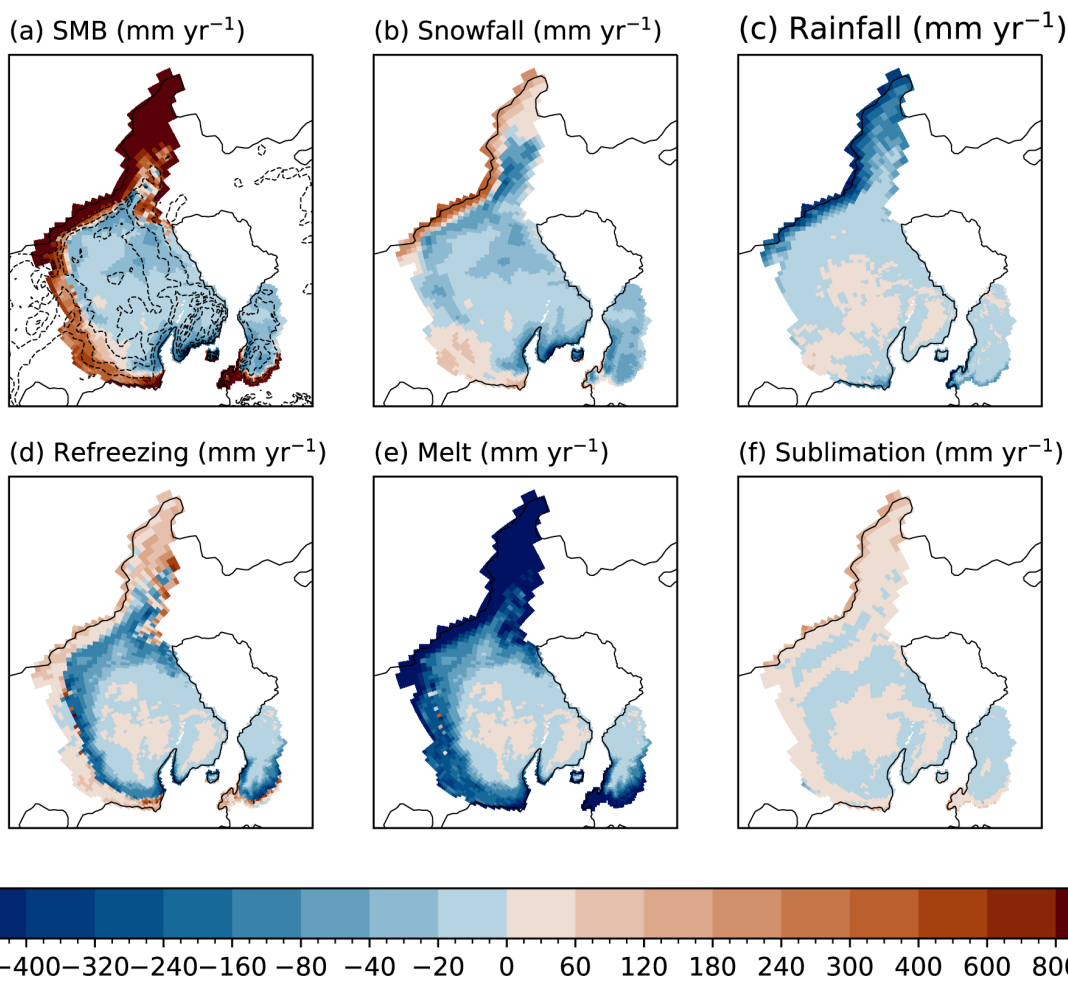
Figure 10. Difference between the results of the LG-26ka and LG-21ka (annual means from the last 20 years of each simulation). (a) surface mass balance, (b) snowfall, (c) rainfall, (d) refreezing, (e) melt, and (f) sublimation, all in mm yr^{-1}.

5 Discussion and conclusions

Here, we present for the first time a detailed, explicit analysis of climate, SMB and energy components over northern hemisphere ice sheets, with a similar approach as adopted for modern ice sheets with regional climate models (Ettema et al., 2010, 2009; Noël et al., 2018, 2020) and projections with global climate models (Muntjewerf et al., 2020a). This detailed analysis of surface mass and energy components is meant to facilitate an advanced comparison of climate and ice sheet simulations between (multiple) past and future time periods. A direct evaluation of our simulated SMB and components is not straightforward as there are no direct proxies available for the LGM, except for snowfall accumulation rates over the GrIS. Therefore, here we will briefly compare our results with Kapsch et al. (2021), who presented results of the spatial distribution of the SMB of the Northern Hemisphere ice sheets during the last deglaciation. In their study, they downscale their results to two different ice sheet reconstructions; ICE6G (Peltier et al., 2015) and GLAC1D (Tarasov et al., 2012). Our simulated LG-21ka SMB spatial distribution is largely similar to Kapsch et al. (2021) downscaled onto the GLAC1D topography (this topography is the same for the NAISC in both studies) (Fig. 8 and Kapsch et al. (2021) figure 4). The simulation over common accumulation areas is very similar, with precipitation maxima over the CIS and southwestern Laurentide and southern Scandinavian, and minima over present-day Hudson Bay, northern half of Greenland and the BKIS. The width of our ablation areas is difficult to compare as we present results on the climate (land component) grid while Kapsch et al. (2021) are on a higher resolution grid. However, in general the distribution of ablation areas is very similar, with the major discrepancy being we have a larger ablation area for the BIIS that in their case. This discrepancy is smaller if we compare with their SMB downscaled to the ICE6G reconstruction (their Figure A2). For the Scandinavian and BKIS, our ablation area simulation is closest to Kapsch et al. (2021) downscaled to the GLAC-1D topography.

Our simulated SMB for the NAISC appears too negative to prevent large marginal retreat if used as forcing for an ice sheet dynamical model. This suggests that one or more of this could explain this low SMB: a) biases in the climate and/or snow/firn simulation, b) biases in the ice sheet reconstruction (as the SMB is largely dependent on surface topography), c) climate and SMB conditions largely out of equilibrium during the LGM. In following work, we will apply the simulated SMB as forcing for an ice sheet model to simulate ice sheet flow during the LGM.

Data availability. The Osman et al. (2021) data was downloaded from: https://www.ncdc.noaa.gov/paleo/study/33112. The Paul et al. (2021) was downloaded from: https://doi.org/10.1594/PANGAEA.923262

Appendix A: Ice sheet reconstruction
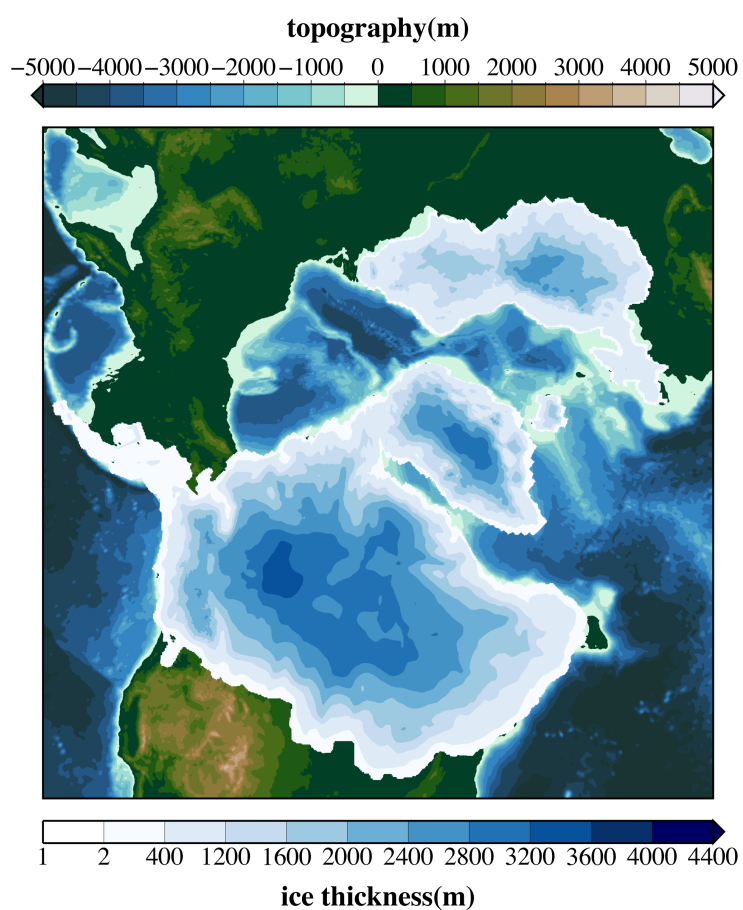
Figure A1. Ice sheet reconstructions used for simulations LG-21ka and LG-26ka at the finer CISM2.1 grid that is used for the elevation classes calculation of the surface mass balance. The reconstruction combines the Antarctic and Patagonia ice sheets from ICE5G (Peltier, 2004), the North American ice sheet complex (Laurentide, Cordilleran and Innuitian) (Tarasov et al., 2012), Greenland ice sheet (Lecavalier et al., 2014) and the Eurasian ice sheet complex (British and Irish, Scandinavian and Barents-Kara Sea) from BRITICE-CHRONO (Clark et al., 2021)

Appendix B: Generation of input paleovegetation dataset

An offline vegetation model (BIOME4, https://github.com/jedokaplan/BIOME4, Kaplan et al. (2003)) was ran using climate forcing of LG-21ka simulation to generate a LGM vegetation distribution. This simulated LGM vegetation distribution was combined with a present-day vegetation dataset as follows:

• The CLM5 standard present-day vegetation dataset Lawrence et al. (2019) is prescribed over the Southern Hemisphere and at low latitudes in the Northern Hemisphere. In these locations, the present-day vegetation is extrapolated over LGM emerged land using a nearest-neighbor mapping algorithm.

• At higher latitudes in the Northern Hemisphere (North of 35 N in Europe and Asia, North of 20 N in North America) we prescribe a LGM vegetation based on the BIOME4 stand-alone simulation, which is run on a 0.5-degree global grid, and is forced with:

– monthly-averaged surface temperature, precipitation and cloudiness for the last 20 years of a 90 years-long CESM2 LGM simulation using the standard present-day vegetation dataset;

– LGM CO2, and orbitals (as in the CESM2 LGM simulation 21ka);

– LGM soil properties dataset, provided as a personnal communication by J. Kaplan.

The LGM BIOME4-simulated vegetation types are converted into CLM5 Plant Functional Types (PFTs) following the conversion table 2.1 in Oleson et al. (2013). Moreover, the following additional corrections are applied:

• Boreal brodleaf deciduous shrubs and boreal grass are prescribed over the Siberian continental shelf;

• Tropical broadleaf evergreen trees north of 20 N have been converted to temperate broadleaf evergreen trees.

In Fig. B1, we show maps of the PFT percentage in the hybrid LGM/present-day vegetation dataset, whereas in Fig. B2 we show the output of the LGM BIOME4 simulation.
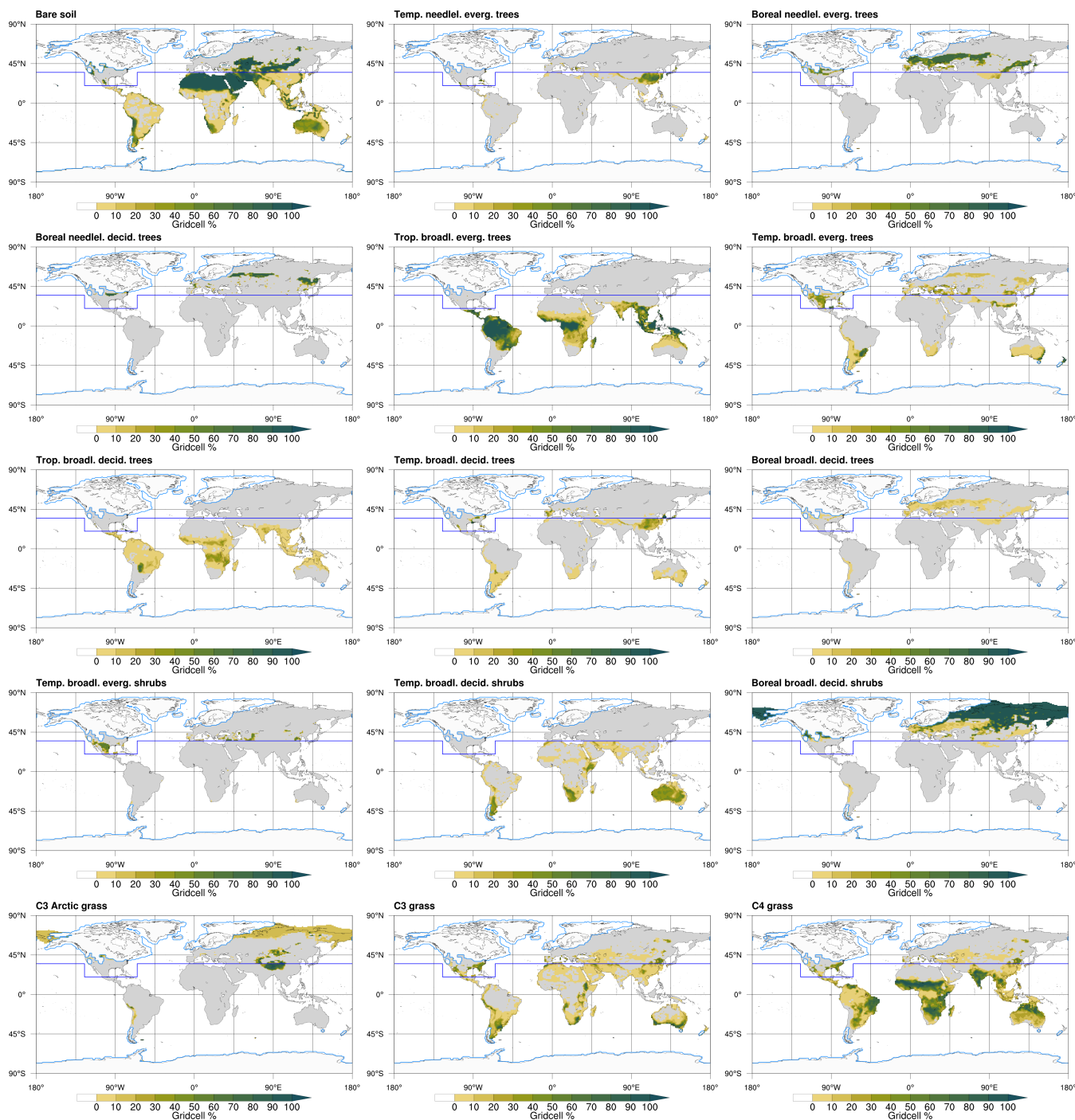
Figure B1. Global map of percentage of land cover, for each CLM5 Plant Functional Type (PFT), in the hybrid LGM/present-day vegetation dataset. The dark blue line indicates the latitude limit above which the LGM BIOME4-based vegetation is used, instead of the standard CLM5 present-day vegetation dataset (which is prescribed below the latitude limit).
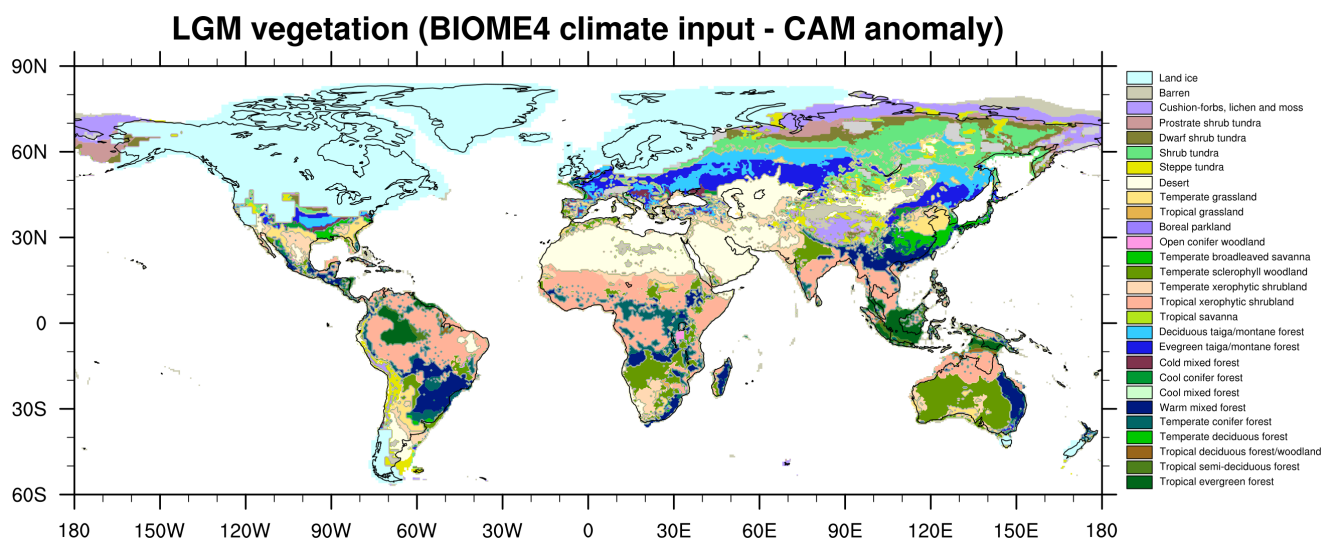
Figure B2. Simulated vegetation types in the BIOME4 stand-alone simulation.
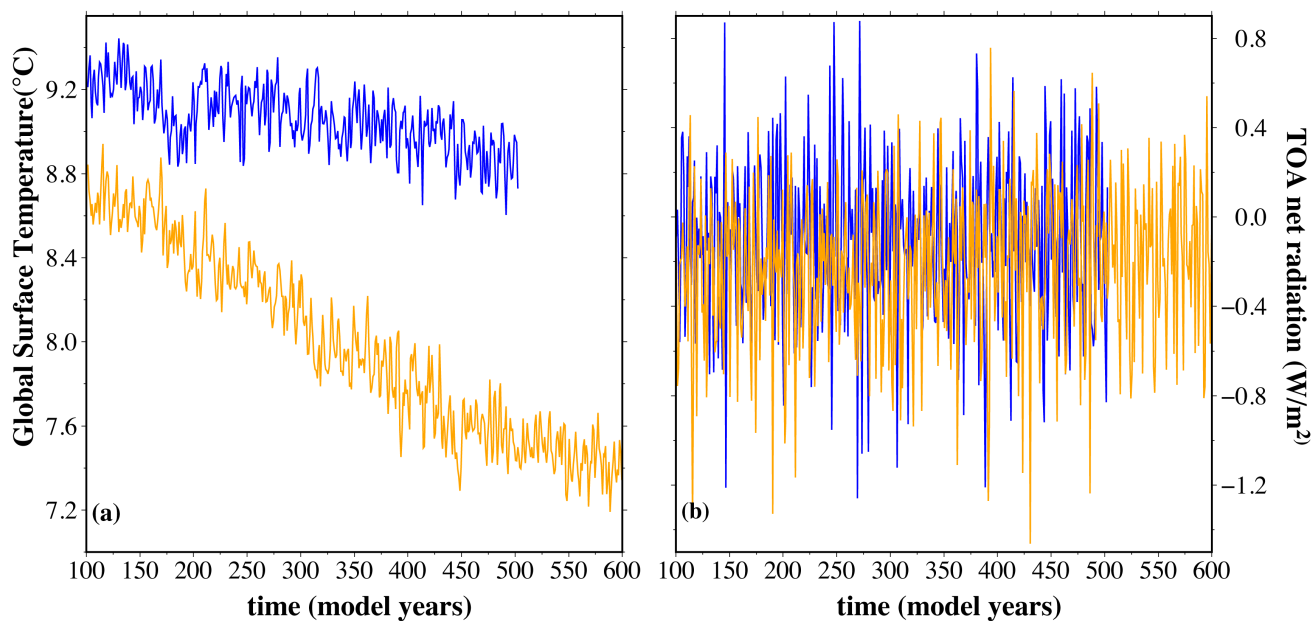
Figure C1. (a) Global surface temperature (°C) from LG-21ka (blue line) and LG-26ka (orange line). (b) Top of the atmosphere (TOA) net radiation (W/m2) for LG-21ka (blue line) and LG-26ka (orange line)

.

395   **Appendix C: Simulated climate**
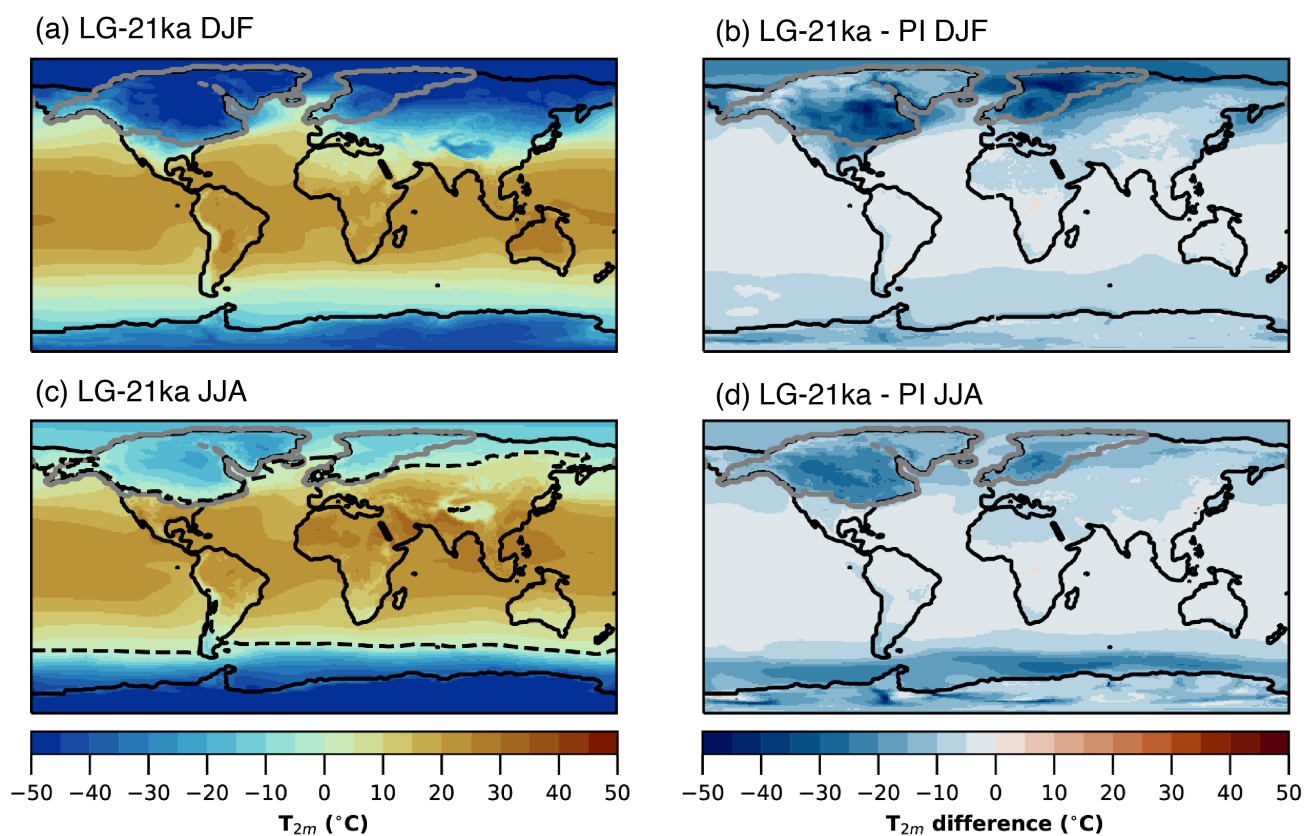
Figure C2. Near-surface temperature. a) and b) shows for DJF, while c) and d) shows for JJA, all in °C. The left column shows values from the LG-21ka simulation, while the right column shows the differences between LG-21ka and the PI simulations. Grey contour encloses glaciated areas (>50% ice cover). The black dashed line in c) follows the 0°C isotherms
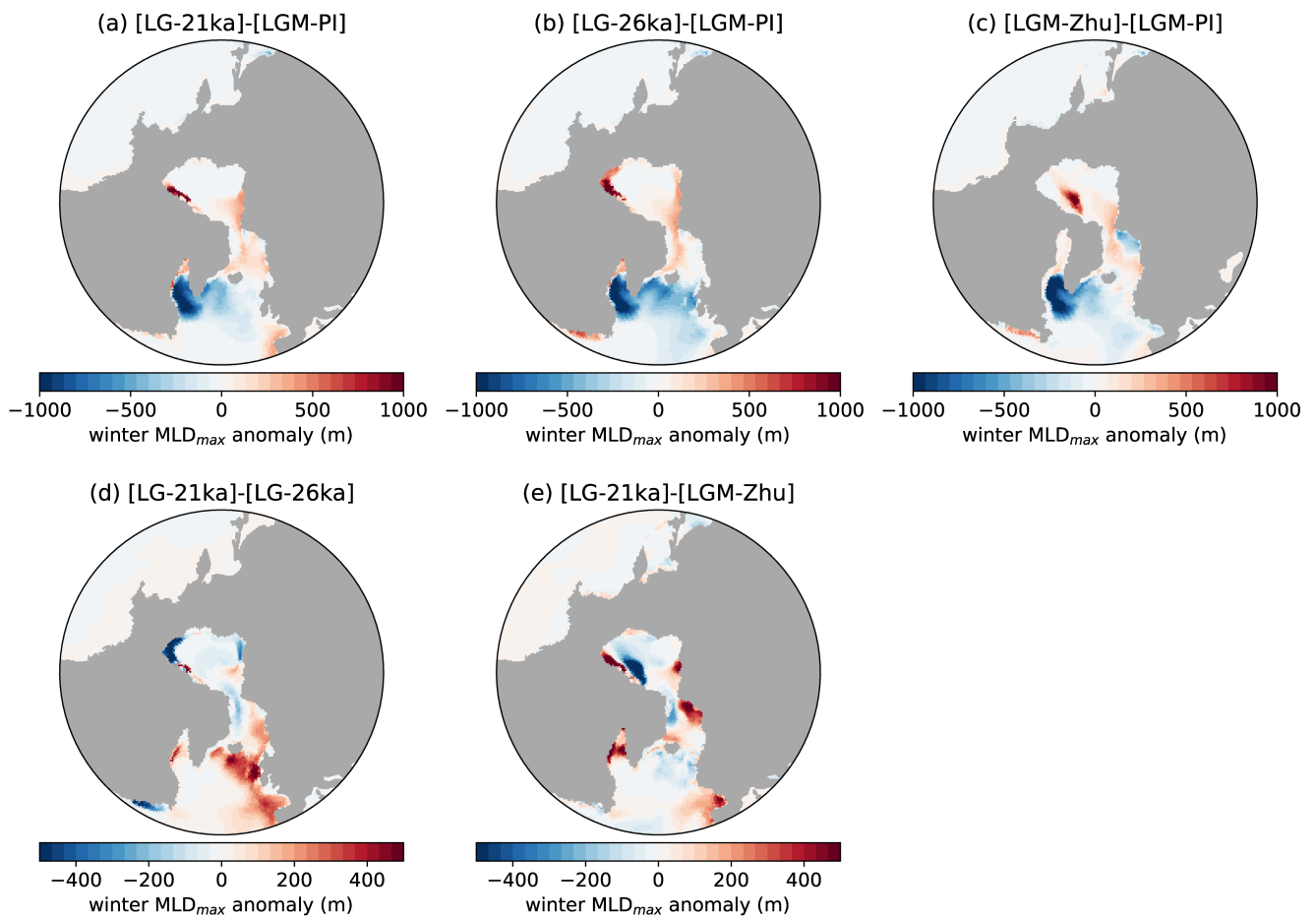
Figure C3. Anomaly of the local maximum of the mixed layer depth during wintertime (in m) for (a) LG-21ka, (b) LG-26ka and (c) LGM-Zhu with respect to the LGM-PI simulation and for LG-21ka with respect to (d) LG-26ka and (e) LGM-Zhu.
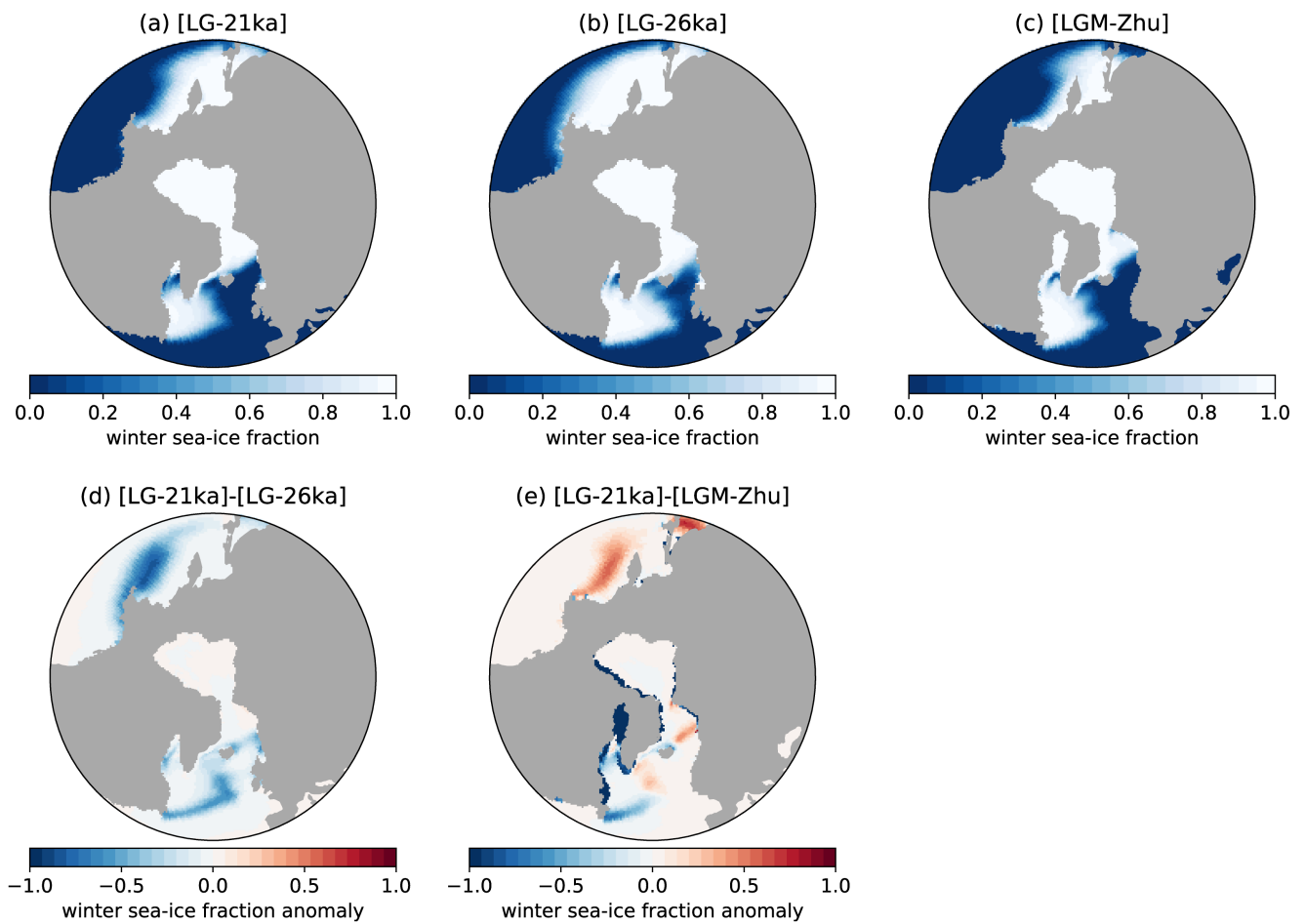
Figure C4. Sea ice fraction during wintertime for (a) LG-21ka, (b) LG-26ka and (c) LGM-Zhu. Winter sea ice fraction anomaly for LG-21ka with respect to (d) LG-26ka and (e) LGM-Zhu.

Author contributions. SB and MP designed the simulations and prepared initial and boundary conditions, SB and RS ran the simulations. RS, SB and SG analysed the simulated climate, RS and MV analysed the simulated SMB. JZ and BOB assessed modelling choices as the choice of CAM5 over CAM6. ML provided model grids. SB, RS, SG, MP and MV wrote the manuscript. MV supervised the project and SB coordinated the writing of the manuscript. All authors read the text and provided comments.

400 *Competing interests.* The authors declare that there are no competing interests

Acknowledgements. R.S., M.P., M.V. and S.G. acknowledge funding from the ERC Starting Grant CoupledIceClim 678145. S.L.B. has received support from the European Research Council (ERC) under the European Union's Horizon 2020 research and innovation programme (ERC Advanced Grant PALGLAC 787263). The CESM project is supported primarily by the National Science Foundation (NSF). This material is based upon work supported by the National Center for Atmospheric Research, which is a major facility sponsored by the NSF under
405 Cooperative Agreement No. 1852977. The authors thank J. Kaplan for providing the LGM soil properties dataset and for his suggestions on the setup of the BIOME4 LGM vegetation simulation.

References

Bereiter, B., Sarah, E., Jochen, S., Christoph, N.-A., F., S. T., Hubertus, F., Sepp, K., and Jerome, C.: Revision of the EPICA Dome C CO2 record from 800 to 600 kyr before present, Geophysical Research Letters, 42, 542–549, https://doi.org/https://doi.org/10.1002/2014GL061957, 2015.

Berger, A.: Long-Term Variations of Daily Insolation and Quaternary Climatic Changes, Journal of Atmospheric Sciences, 35, 2362–2367, https://doi.org/10.1175/1520-0469(1978)035<2362:LTVODI>2.0.CO;2, 1978.

Brady, E. C., Otto-Bliesner, B. L., Kay, J. E., and Rosenbloom, N.: Sensitivity to Glacial Forcing in the CCSM4, Journal of Climate, 26, 1901 – 1925, https://doi.org/10.1175/JCLI-D-11-00416.1, 2013.

Clark, C. D., Chiverrell, R. C., Fabel, D., Hindmarsh, R. C. A., Ó Cofaigh, C., and Scourse, J. D.: Timing, pace and controls on ice sheet retreat: an introduction to the BRITICE-CHRONO transect reconstructions of the British–Irish Ice Sheet, Journal of Quaternary Science, 36, 673–680, https://doi.org/https://doi.org/10.1002/jqs.3326, https://doi.org/10.1002/jqs.3326, 2021.

Clark, C. D., Ely, J. C., Hindmarsh, R. C. A., Bradley, S., Ignéczi, A., Fabel, D., Ó Cofaigh, C., Chiverrell, R. C., Scourse, J., Benetti, S., Bradwell, T., Evans, D. J. A., Roberts, D. H., Burke, M., Callard, S. L., Medialdea, A., Saher, M., Small, D., Smedley, R. K., Gasson, E., Gregoire, L., Gandy, N., Hughes, A. L. C., Ballantyne, C., Bateman, M. D., Bigg, G. R., Doole, J., Dove, D., Duller, G. A. T., Jenkins, G. T. H., Livingstone, S. L., McCarron, S., Moreton, S., Pollard, D., Praeg, D., Sejrup, H. P., Van Landeghem, K. J. J., and Wilson, P.: Growth and retreat of the last British–Irish Ice Sheet, 31 000 to 15 000 years ago: the BRITICE-CHRONO reconstruction, Boreas, 51, 699–758, https://doi.org/https://doi.org/10.1111/bor.12594, 2022.

Clark, P. U., Dyke, A. S., Shakun, J. D., Carlson, A. E., Clark, J., Wohlfart, h. B., Mitrovica, J. X., Hostetler, S. W., and McCabe, A. M.: The Last Glacial Maximum, Science, 325, 710–714, https://doi.org/10.1126/science.1172873, doi: 10.1126/science.1172873, 2009.

Dalton, A. S., Stokes, C. R., and Batchelor, C. L.: Evolution of the Laurentide and Innuitian ice sheets prior to the Last Glacial Maximum (115 ka to 25 ka), Earth-Science Reviews, 224, 103 875, https://doi.org/https://doi.org/10.1016/j.earscirev.2021.103875, 2022.

Danabasoglu, G., G., L. W., and P., B. B.: Climate impacts of parameterized Nordic Sea overflows, Journal of Geophysical Research: Oceans, 115, https://doi.org/https://doi.org/10.1029/2010JC006243, 2010.

Danabasoglu, G., Lamarque, J. F., Bacmeister, J., Bailey, D. A., DuVivier, A. K., Edwards, J., Emmons, L. K., Fasullo, J., Garcia, R., Gettelman, A., Hannay, C., Holland, M. M., Large, W. G., Lauritzen, P. H., Lawrence, D. M., Lenaerts, J. T. M., Lindsay, K., Lipscomb, W. H., Mills, M. J., Neale, R., Oleson, K. W., Otto-Bliesner, B., Phillips, A. S., Sacks, W., Tilmes, S., van Kampenhout, L., Vertenstein, M., Bertini, A., Dennis, J., Deser, C., Fischer, C., Fox-Kemper, B., Kay, J. E., Kinnison, D., Kushner, P. J., Larson, V. E., Long, M. C., Mickelson, S., Moore, J. K., Nienhouse, E., Polvani, L., Rasch, P. J., and Strand, W. G.: The Community Earth System Model Version 2 (CESM2), Journal of Advances in Modeling Earth Systems, 12, e2019MS001 916, https://doi.org/https://doi.org/10.1029/2019MS001916, 2020.

DiNezio, P. N., Tierney, J. E., Otto-Bliesner, B. L., Timmermann, A., Bhattacharya, T., Rosenbloom, N., and Brady, E.: Glacial changes in tropical climate amplified by the Indian Ocean, Science Advances, 4, eaat9658, https://doi.org/10.1126/sciadv.aat9658, 2018.

Dunmire, D., Lenaerts, J. T. M., Datta, R. T., and Gorte, T.: Antarctic surface climate and surface mass balance in the Community Earth System Model version 2 during the satellite era and into the future (1979–2100), The Cryosphere, 16, 4163–4184, https://doi.org/10.5194/tc-16-4163-2022, 2022.

Ettema, J., van den Broeke, M. R., van Meijgaard, E., van de Berg, W. J., Bamber, J. L., Box, J. E., and Bales, R. C.: Higher surface mass balance of the Greenland ice sheet revealed by high-resolution climate modeling, Geophysical Research Letters, 36, https://doi.org/https://doi.org/10.1029/2009GL038110, 2009.

445 Ettema, J., van den Broeke, M. R., van Meijgaard, E., and van de Berg, W. J.: Climate of the Greenland ice sheet using a high-resolution climate model – Part 2: Near-surface climate and energy balance, The Cryosphere, 4, 529–544, https://doi.org/10.5194/tc-4-529-2010, 2010.

Fyke, J., Sergienko, O., Lofverstrom, M., Price, S., and Lenaerts, J. T. M.: An Overview of Interactions and Feedbacks Between Ice Sheets and the Earth System, Reviews of Geophysics, 56, 361–408, https://doi.org/https://doi.org/10.1029/2018RG000600, 2018.

450 Gettelman, A., Hannay, C., Bacmeister, J. T., Neale, R. B., Pendergrass, A. G., Danabasoglu, G., Lamarque, J.-F., Fasullo, J. T., Bailey, D. A., Lawrence, D. M., and Mills, M. J.: High Climate Sensitivity in the Community Earth System Model Version 2 (CESM2), Geophysical Research Letters, 46, 8329–8337, https://doi.org/https://doi.org/10.1029/2019GL083978, 2019.

Gu, S., Liu, Z., Oppo, D. W., Lynch-Stieglitz, J., Jahn, A., Zhang, J., and Wu, L.: Assessing the potential capability of reconstructing glacial Atlantic water masses and AMOC using multiple proxies in CESM, Earth and Planetary Science Letters, 541,
455 https://doi.org/10.1016/j.epsl.2020.116294, 2020.

Hughes, A. L. C., Richard., G., Øystein S., L., Jan., M., and Inge, S. J.: The last Eurasian ice sheets – a chronological database and time-slice reconstruction, DATED-1, Boreas, 45, 1–45, https://doi.org/https://doi.org/10.1111/bor.12142, 2016.

Hurrell, J. W., Holland, M. M., Gent, P. R., Ghan, S., Kay, J. E., Kushner, P. J., Lamarque, J.-F., Large, W. G., Lawrence, D., Lindsay, K., Lipscomb, W. H., Long, M. C., Mahowald, N., Marsh, D. R., Neale, R. B., Rasch, P., Vavrus, S., Vertenstein, M., Bader, D., Collins, W. D.,
460 Hack, J. J., Kiehl, J., and Marshall, S.: The Community Earth System Model: A Framework for Collaborative Research, Bulletin of the American Meteorological Society, 94, 1339 – 1360, https://doi.org/10.1175/BAMS-D-12-00121.1, 2013.

Ivanovic, R. F., Gregoire, L. J., Kageyama, M., Roche, D. M., Valdes, P. J., Burke, A., Drummond, R., Peltier, W. R., and Tarasov, L.: Transient climate simulations of the deglaciation 21-9 thousand years before present (version 1) - PMIP4 Core experiment design and boundary conditions, Geoscientific Model Development, 9, 2563–2587, https://doi.org/10.5194/gmd-9-2563-2016, 2016.

465 Kageyama, M., Albani, S., Braconnot, P., Harrison, S. P., Hopcroft, P. O., Ivanovic, R. F., Lambert, F., Marti, O., Peltier, W. R., Peterschmitt, J. Y., Roche, D. M., Tarasov, L., Zhang, X., Brady, E. C., Haywood, A. M., LeGrande, A. N., Lunt, D. J., Mahowald, N. M., Mikolajewicz, U., Nisancioglu, K. H., Otto-Bliesner, B. L., Renssen, H., Tomas, R. A., Zhang, Q., Abe-Ouchi, A., Bartlein, P. J., Cao, J., Li, Q., Lohmann, G., Ohgaito, R., Shi, X., Volodin, E., Yoshida, K., and Zheng, W.: The PMIP4 contribution to CMIP6 – Part 4: Scientific objectives and experimental design of the PMIP4-CMIP6 Last Glacial Maximum experiments and PMIP4 sensitivity experiments, Geosci. Model Dev.,
470 10, 4035–4055, https://doi.org/10.5194/gmd-10-4035-2017, gMD, 2017.

Kageyama, M., Harrison, S. P., Kapsch, M. L., Lofverstrom, M., Lora, J. M., Mikolajewicz, U., Sherriff-Tadano, S., Vadsaria, T., Abe-Ouchi, A., Bouttes, N., Chandan, D., Gregoire, L. J., Ivanovic, R. F., Izumi, K., Legrande, A. N., Lhardy, F., Lohmann, G., Morozova, P. A., Ohgaito, R., Paul, A., Peltier, W. R., Poulsen, C. J., Quiquet, A., Roche, D. M., Shi, X., Tierney, J. E., Valdes, P. J., Volodin, E., and Zhu, J.: The PMIP4 Last Glacial Maximum experiments: Preliminary results and comparison with the PMIP3 simulations, Climate of the Past,
475 17, 1065–1089, https://doi.org/10.5194/cp-17-1065-2021, 2021.

Kaplan, J. O., Bigelow, N. H., Prentice, I. C., Harrison, S. P., Bartlein, P. J., Christensen, T. R., Cramer, W., Matveyeva, N. V., McGuire, A. D., Murray, D. F., Razzhivin, V. Y., Smith, B., Walker, D. A., Anderson, P. M., Andreev, A. A., Brubaker, L. B., Edwards, M. E., and Lozhkin, A. V.: Climate change and Arctic ecosystems: 2. Modeling, paleodata-model comparisons, and future projections, Journal of Geophysical Research: Atmospheres, 108, https://doi.org/https://doi.org/10.1029/2002JD002559, 2003.

480   Kapsch, M.-L., Mikolajewicz, U., Ziemen, F. A., Rodehacke, C. B., and Schannwell, C.: Analysis of the surface mass balance for deglacial climate simulations, The Cryosphere, 15, 1131–1156, https://doi.org/10.5194/tc-15-1131-2021, 2021.

Kapsch, M.-L., Mikolajewicz, U., Ziemen, F., and Schannwell, C.: Ocean Response in Transient Simulations of the Last Deglaciation Dominated by Underlying Ice-Sheet Reconstruction and Method of Meltwater Distribution, Geophysical Research Letters, 49, e2021GL096 767, https://doi.org/https://doi.org/10.1029/2021GL096767, https://doi.org/10.1029/2021GL096767, 2022.

485   Klockmann, M., Mikolajewicz, U., and Marotzke, J.: American Meteorological Society Two AMOC States in Response to Decreasing Greenhouse Gas Concentrations in the Coupled Climate Model MPI-ESM, Source: Journal of Climate, 31, 7969–7984, https://doi.org/10.2307/26496703, 2018.

Lawrence, D. M., Fisher, R. A., Koven, C. D., Oleson, K. W., Swenson, S. C., Bonan, G., Collier, N., Ghimire, B., van Kampenhout, L., Kennedy, D., Kluzek, E., Lawrence, P. J., Li, F., Li, H., Lombardozzi, D., Riley, W. J., Sacks, W. J., Shi, M., Vertenstein, M., Wieder,
490   W. R., Xu, C., Ali, A. A., Badger, A. M., Bisht, G., van den Broeke, M., Brunke, M. A., Burns, S. P., Buzan, J., Clark, M., Craig, A., Dahlin, K., Drewniak, B., Fisher, J. B., Flanner, M., Fox, A. M., Gentine, P., Hoffman, F., Keppel-Aleks, G., Knox, R., Kumar, S., Lenaerts, J., Leung, L. R., Lipscomb, W. H., Lu, Y., Pandey, A., Pelletier, J. D., Perket, J., Randerson, J. T., Ricciuto, D. M., Sanderson, B. M., Slater, A., Subin, Z. M., Tang, J., Thomas, R. Q., Val Martin, M., and Zeng, X.: The Community Land Model Version 5: Description of New Features, Benchmarking, and Impact of Forcing Uncertainty, Journal of Advances in Modeling Earth Systems, 11, 4245–4287,
495   https://doi.org/https://doi.org/10.1029/2018MS001583, 2019.

Lecavalier, B. S., Milne, G. A., Simpson, M. J. R., Wake, L., Huybrechts, P., Tarasov, L., Kjeldsen, K. K., Funder, S., Long, A. J., Woodroffe, S., Dyke, A. S., and Larsen, N. K.: A model of Greenland ice sheet deglaciation constrained by observations of relative sea level and ice extent, Quaternary Science Reviews, 102, 54–84, https://doi.org/https://doi.org/10.1016/j.quascirev.2014.07.018, 2014.

Lenaerts, J. T. M., Medley, B., van den Broeke, M. R., and Wouters, B.: Observing and Modeling Ice Sheet Surface Mass Balance, Reviews
500   of Geophysics, 57, 376–420, https://doi.org/https://doi.org/10.1029/2018RG000622, 2019.

Lipscomb, W. H., Price, S. F., Hoffman, M. J., Leguy, G. R., Bennett, A. R., Bradley, S. L., Evans, K. J., Fyke, J. G., Kennedy, J. H., Perego, M., Ranken, D. M., Sacks, W. J., Salinger, A. G., Vargo, L. J., and Worley, P. H.: Description and evaluation of the Community Ice Sheet Model (CISM) v2.1, Geoscientific Model Development, 12, 387–424, https://doi.org/10.5194/gmd-12-387-2019, 2019.

Lofverstrom, M., Fyke, J., Thayer-Calder, K., Muntjewerf, L., Vizcaino, M., Sacks, W. J., Lipscomb, W. H., Otto-Bliesner, B., and Bradley,
505   S. L.: An efficient ice-sheet/Earth system model spin-up procedure for CESM2.1 and CISM2.1: description, evaluation, and broader applicability, Journal of Advances in Modeling Earth Systems, 12, e2019MS001 984, https://doi.org/10.1029/2019MS001984, 2020.

Lofverstrom, M., Thompson, D. M., Otto-Bliesner, B. L., and Brady, E. C.: The importance of Canadian Arctic Archipelago gateways for glacial expansion in Scandinavia, Nature Geoscience, 15, 482–488, https://doi.org/10.1038/s41561-022-00956-9, 2022.

Loulergue, L., Schilt, A., Spahni, R., Masson-Delmotte, V., Blunier, T., Lemieux, B., Barnola, J.-M., Raynaud, D., Stocker, T. F.,
510   and Chappellaz, J.: Orbital and millennial-scale features of atmospheric CH4 over the past 800,000 years, Nature, 453, 383–386, https://doi.org/10.1038/nature06950, 2008.

Mix, A. C., Bard, E., and Schneider, R.: Environmental processes of the ice age: land, oceans, glaciers (EPILOG), Quaternary Science Reviews, 20, 627–657, https://doi.org/https://doi.org/10.1016/S0277-3791(00)00145-1, 2001.

Mottram, R., Hansen, N., Kittel, C., van Wessem, J. M., Agosta, C., Amory, C., Boberg, F., van de Berg, W. J., Fettweis, X., Gossart, A., van
515   Lipzig, N. P. M., van Meijgaard, E., Orr, A., Phillips, T., Webster, S., Simonsen, S. B., and Souverijns, N.: What is the surface mass balance of Antarctica? An intercomparison of regional climate model estimates, The Cryosphere, 15, 3751–3784, https://doi.org/10.5194/tc-15-3751-2021, 2021.

Muglia, J. and Schmittner, A.: Carbon isotope constraints on glacial Atlantic meridional overturning: Strength vs depth, Quaternary Science Reviews, 257, 106 844, https://doi.org/https://doi.org/10.1016/j.quascirev.2021.106844, 2021.

520   Muntjewerf, L., Petrini, M., Vizcaino, M., da Silva, C. E., Sellevold, R., Scherrenberg, M. D., Thayer-Calder, K., Bradley, S. L., Lenaerts, J. T., Lipscomb, W. H., and Lofverstrom, M.: Greenland Ice Sheet Contribution to 21st Century Sea Level Rise as Simulated by the Coupled CESM2.1-CISM2.1, Geophysical Research Letters, 47, https://doi.org/10.1029/2019GL086836, 2020a.

Muntjewerf, L., Sellevold, R., Vizcaino, M., da Silva, C. E., Petrini, M., Thayer-Calder, K., Scherrenberg, M. D., Bradley, S. L., Katsman, C. A., Fyke, J., Lipscomb, W. H., Lofverstrom, M., and Sacks, W. J.: Accelerated Greenland Ice Sheet Mass Loss Under High

525   Greenhouse Gas Forcing as Simulated by the Coupled CESM2.1-CISM2.1, Journal of Advances in Modeling Earth Systems, 12, https://doi.org/10.1029/2019MS002031, 2020b.

Muntjewerf, L., Sacks, W. J., Lofverstrom, M., Fyke, J., Lipscomb, W. H., Ernani da Silva, C., Vizcaino, M., Thayer-Calder, K., Lenaerts, J. T. M., and Sellevold, R.: Description and Demonstration of the Coupled Community Earth System Model v2 – Community Ice Sheet Model v2 (CESM2-CISM2), Journal of Advances in Modeling Earth Systems, 13, e2020MS002 356, 2021.

530   Noël, B., van de Berg, W. J., van Wessem, J. M., van Meijgaard, E., van As, D., Lenaerts, J. T. M., Lhermitte, S., Kuipers Munneke, P., Smeets, C. J. P. P., van Ulft, L. H., van de Wal, R. S. W., and van den Broeke, M. R.: Modelling the climate and surface mass balance of polar ice sheets using RACMO2 – Part 1: Greenland (1958–2016), The Cryosphere, 12, 811–831, https://doi.org/10.5194/tc-12-811-2018, 2018.

Noël, B., van Kampenhout, L., van de Berg, W. J., Lenaerts, J. T. M., Wouters, B., and van den Broeke, M. R.: Brief communica-

535   tion: CESM2 climate forcing (1950–2014) yields realistic Greenland ice sheet surface mass balance, The Cryosphere, 14, 1425–1435, https://doi.org/10.5194/tc-14-1425-2020, 2020.

Oleson, K., Lawrence, D. M., Bonan, G. B., Drewniak, B., Huang, M., Koven, C. D., Levis, S., Li, F., Riley, W. J., Subin, Z. M., Swenson, S. C., Thornton, P. E., Bozbiyik, A., Fisher, R., Heald, C. L., Kluzek, E., Lamarque, J.-F., Lawrence, P. J., Leung, L. R., Lipscomb, W., Muszala, S., Ricciuto, D. M., Sacks, W., Sun, Y., Tang, J., and Yang, Z.-L.: Technical description of version 4.5 of the Community Land

540   Model (CLM), NCAR Tech. Note NCAR/TN-503 + STR, 2013.

Osman, M. B., Tierney, J. E., Zhu, J., Tardif, R., Hakim, G. J., King, J., and Poulsen, C. J.: Globally resolved surface temperatures since the Last Glacial Maximum, Nature, 599, 239–244, https://doi.org/10.1038/s41586-021-03984-4, 2021.

Patton, H., Hubbard, A., Andreassen, K., Winsborrow, M., and Stroeven, A. P.: The build-up, configuration, and dynamical sensitivity of the Eurasian ice-sheet complex to Late Weichselian climatic and oceanic forcing, Quaternary Science Reviews, 153, 97–121,

545   https://doi.org/https://doi.org/10.1016/j.quascirev.2016.10.009, 2016.

Paul, A., Mulitza, S., Stein, R., and Werner, M.: A global climatology of the ocean surface during the Last Glacial Maximum mapped on a regular grid (GLOMAP), Clim. Past, 17, 805–824, https://doi.org/10.5194/cp-17-805-2021, cP, 2021.

Peltier, W. R.: GLOBAL GLACIAL ISOSTASY AND THE SURFACE OF THE ICE-AGE EARTH: The ICE-5G (VM2) Model and GRACE, Annual Review of Earth and Planetary Sciences, 32, 111–149, https://doi.org/10.1146/annurev.earth.32.082503.144359, doi:

550   10.1146/annurev.earth.32.082503.144359, 2004.

Peltier, W. R., F., A. D., and R., D.: Space geodesy constrains ice age terminal deglaciation: The global ICE-6G_C (VM5a) model, Journal of Geophysical Research: Solid Earth, 120, 450–487, https://doi.org/https://doi.org/10.1002/2014JB011176, 2015.

Petit, J. R., Jouzel, J., Raynaud, D., Barkov, N. I., Barnola, J. M., Basile, I., Bender, M., Chappellaz, J., Davis, M., Delaygue, G., Delmotte, M., Kotlyakov, V. M., Legrand, M., Lipenkov, V. Y., Lorius, C., PÉpin, L., Ritz, C., Saltzman, E., and Stievenard, M.: Climate and

555   atmospheric history of the past 420,000 years from the Vostok ice core, Antarctica, Nature, 399, 429–436, https://doi.org/10.1038/20859, 1999.

Quiquet, A., Roche, D. M., Dumas, C., Bouttes, N., and Lhardy, F.: Climate and ice sheet evolutions from the last glacial maximum to the pre-industrial period with an ice-sheet–climate coupled model, Clim. Past, 17, 2179–2199, https://doi.org/10.5194/cp-17-2179-2021, cP, 2021.

560   Schilt, A., Baumgartner, M., Schwander, J., Buiron, D., Capron, E., Chappellaz, J., Loulergue, L., Schüpbach, S., Spahni, R., Fischer, H., and Stocker, T. F.: Atmospheric nitrous oxide during the last 140,000years, Earth and Planetary Science Letters, 300, 33–43, https://doi.org/https://doi.org/10.1016/j.epsl.2010.09.027, 2010.

Sellevold, R. and Vizcaíno, M.: Global Warming Threshold and Mechanisms for Accelerated Greenland Ice Sheet Surface Mass Loss, Journal of Advances in Modeling Earth Systems, 12, https://doi.org/10.1029/2019MS002029, 2020.

565   Sellevold, R., Kampenhout, L. V., Lenaerts, J. T., Noël, B., Lipscomb, W. H., and Vizcaino, M.: Surface mass balance downscaling through elevation classes in an Earth system model: Application to the Greenland ice sheet, Cryosphere, 13, 3193–3208, https://doi.org/10.5194/tc-13-3193-2019, 2019.

Sherriff-Tadano, S. and Abe-Ouchi, A.: Roles of Sea Ice–Surface Wind Feedback in Maintaining the Glacial Atlantic Meridional Overturning Circulation and Climate, Journal of Climate, 33, 3001–3018, https://doi.org/10.1175/JCLI-D-19-0431.1, 2020.

570   Sherriff-Tadano, S., Abe-Ouchi, A., Yoshimori, M., Oka, A., and Chan, W.-L.: Influence of glacial ice sheets on the Atlantic meridional overturning circulation through surface wind change, Climate Dynamics, 50, 2881–2903, https://doi.org/10.1007/s00382-017-3780-0, 2018.

Sommers, A. N., L., O.-B. B., H., L. W., Marcus, L., L., S. S., J., B. P., C., B. E., Erik, K., Gunter, L., Katherine, T.-C., and A., T. R.: Retreat and Regrowth of the Greenland Ice Sheet During the Last Interglacial as Simulated by the CESM2-CISM2 Coupled Climate–Ice

575   Sheet Model, Paleoceanography and Paleoclimatology, 36, e2021PA004 272, https://doi.org/https://doi.org/10.1029/2021PA004272, e2021PA004272 2021PA004272, 2021.

Sun, Q., Michael, M. W., Bryan, F. O., and heng Tseng, Y.: A box model for representing estuarine physical processes in Earth system models, Ocean Modelling, 112, 139–153, https://doi.org/https://doi.org/10.1016/j.ocemod.2017.03.004, 2017.

Tarasov, L., Dyke, A. S., Neal, R. M., and Peltier, W. R.: A data-calibrated distribution of deglacial chronologies for

580   the North American ice complex from glaciological modeling, Earth and Planetary Science Letters, 315-316, 30–40, https://doi.org/https://doi.org/10.1016/j.epsl.2011.09.010, 2012.

Tierney, J. E., Zhu, J., King, J., Malevich, S. B., Hakim, G. J., and Poulsen, C. J.: Glacial cooling and climate sensitivity revisited, Nature, 584, 569–573, https://doi.org/10.1038/s41586-020-2617-x, 2020.

van den Broeke, M., Smeets, P., Ettema, J., van der Veen, C., van de Wal, R., and Oerlemans, J.: Partitioning of melt energy and meltwater

585   fluxes in the ablation zone of the west Greenland ice sheet, The Cryosphere, 2, 179–189, https://doi.org/10.5194/tc-2-179-2008, 2008.

van Kampenhout, L., Lenaerts, J. T. M., Lipscomb, W. H., Sacks, W. J., Lawrence, D. M., Slater, A. G., and van den Broeke, M. R.: Improving the Representation of Polar Snow and Firn in the Community Earth System Model, Journal of Advances in Modeling Earth Systems, 9, 2583–2600, https://doi.org/https://doi.org/10.1002/2017MS000988, 2017.

van Kampenhout, L., Lenaerts, J. T. M., Lipscomb, W. H., Lhermitte, S., Noël, B., Vizcaíno, M., Sacks, W. J., and van den Broeke, M. R.:

590   Present-Day Greenland Ice Sheet Climate and Surface Mass Balance in CESM2, Journal of Geophysical Research: Earth Surface, 125, e2019JF005 318, https://doi.org/https://doi.org/10.1029/2019JF005318, 2020.

van Kampenhout, L., Lenaerts, J. T. M., Lipscomb, W. H., Lhermitte, S., Noël, B., Vizcaíno, M., Sacks, W. J., and van den Broeke, M. R.: Present-Day Greenland Ice Sheet Climate and Surface Mass Balance in CESM2, Journal of Geophysical Research: Earth Surface, 125, e2019JF005 318, https://doi.org/https://doi.org/10.1029/2019JF005318, e2019JF005318 10.1029/2019JF005318, 2020.

595 Vizcaíno, M., Lipscomb, W. H., Sacks, W. J., van Angelen, J. H., Wouters, B., and van den Broeke, M. R.: Greenland Surface Mass Balance as Simulated by the Community Earth System Model. Part I: Model Evaluation and 1850–2005 Results, Journal of Climate, 26, 7793–7812, https://doi.org/10.1175/JCLI-D-12-00615.1, 2013.

Whitehouse, P. L.: Glacial isostatic adjustment modelling: historical perspectives, recent advances, and future directions, Earth Surf. Dynam., 6, 401–429, https://doi.org/10.5194/esurf-6-401-2018, eSurf, 2018.

600 Zhu, J., Liu, Z., Zhang, X., Eisenman, I., and Liu, W.: Linear weakening of the AMOC in response to receding glacial ice sheets in CCSM3, Geophysical Research Letters, 41, 6252–6258, 2014.

Zhu, J., Otto-Bliesner, B. L., Brady, E. C., Poulsen, C. J., Tierney, J. E., Lofverstrom, M., and DiNezio, P.: Assessment of Equilibrium Climate Sensitivity of the Community Earth System Model Version 2 Through Simulation of the Last Glacial Maximum, Geophysical Research Letters, 48, e2020GL091 220, https://doi.org/https://doi.org/10.1029/2020GL091220, e2020GL091220 2020GL091220, 2021.

605 Zhu, J., Otto-Bliesner, B. L., Brady, E. C., Gettelman, A., Bacmeister, J. T., Neale, R. B., Poulsen, C. J., Shaw, J. K., McGraw, Z. S., and Kay, J. E.: LGM paleoclimate constraints inform cloud parameterizations and equilibrium climate sensitivity in CESM2, Journal of Advances in Modeling Earth Systems, 14, e2021MS002 776, 2022.

Ziemen, F. A., Rodehacke, C. B., and Mikolajewicz, U.: Coupled ice sheet–climate modeling under glacial and pre-industrial boundary conditions, Clim. Past, 10, 1817–1836, https://doi.org/10.5194/cp-10-1817-2014, cP, 2014.